3D particle-based DEM investigation into the shear behaviour of incipient rock joints with various geometries of rock bridges

J Shang[1], Z Zhao[1], J Hu[2], K Handley[3]

[1]Nanyang Centre for Underground Space, School of Civil and Environmental Engineering, Nanyang Technological University, Singapore

[2]School of Resources and Safety Engineering, Central South University, Changsha 410083, China

[3] School of Earth and Environment, the University of Leeds, Leeds, United Kingdom

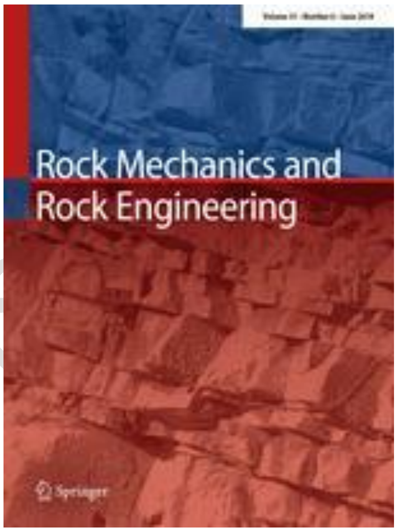

Abstract

A 3D particle-based DEM model was established taking into account the geometries of rock bridges. The model was used to investigate the shear behaviour of incipient rock joints. Fifty-seven direct shear tests were conducted under constant normal load (CNL) boundary conditions using the established model, in which rock bridges with nineteen different geometries and incipient joints with various areal persistence (between 0.2 and 0.96) were involved. Our results show that, for the cases having a single rock bridge, cracks often initiated around the edges of the rock bridges and coalesced first in the middle of the rock bridge areas. While for other cases containing multiple rock bridges, cracks initially appeared at the connection points (located in the middle of the joint planes) of the rock bridges and then propagated to the edges. High crack initiation stresses were measured, which were often more than 60% of the shear strength of the tested incipient rock joints. Sudden failures of the rock bridges subjected to shearing were observed, accompanying dramatic increases in the number of cracks. Another important conclusion derived from this research is that both joint areal persistence and rock bridge geometry played significant roles in the shear failure of the simulated Horton Formation Siltstone joints. The present study has shown that shear strength increased gradually when joint areal persistence was decreased. Interestingly, different shear strength values were measured for rock joints with the same areal persistence (e.g. K=0.5). Shear velocity was also found to have a significant influence on the shear characteristics of the Horton Formation Siltstone joints. A higher shear strength was measured when the shearing velocity was increased from 0.01 to 1 m/s.

Keywords Discrete element method; Particle flow code; Incipient rock joints; Rock bridges; Shear strength; Joint persistence

List of Symbols

A	Cross-sectional area of parallel bond
A_B	Total area of rock bridges on an incipient joint plane
A_{j1}, A_{j2}, ..., A_{jn}	Persistent areas along an incipient joint plane
a, b	Two side lengths of a rectangle rock bridge
c	Cohesion of parallel bond
c_{sj}	Cohesion of smooth-joint bond
d_v, d_h	Vertical and horizontal spacings between adjacent joint planes
E	Young’s modulus

E_c	Young's modulus of particle linear contact
$E_{c\_}$	Young's modulus of parallel bond
F^c	Vector of contact force
F_n	Normal force acting on parallel bond
F_s	Shear force acting on parallel bond
I	Moment of inertia of the cross section of parallel bond
J	Total length of an incipient joint
J^*	Polar moment of inertia of the cross section of parallel bond
$j_1, j_2, ..., j_n$	Joint segments measured along an incipient joint
K	Joint areal persistence
K_n/K_s	Particle linear contact normal to shear stiffness ratio
$K_{n\_}/K_{s\_}$	Parallel bond contact normal to shear stiffness ratio
K_{nsj}	Normal stiffness of smooth joint contact
K_{ssj}	Shear stiffness of smooth joint contact
k	Moment-contribution factor to strength
L^c	Branch vector
N_c	The number of active contacts within the measurement region
R	A property of the cross-section of parallel-bond
R_{max}	Maximum particle radius
R_{min}	Minimum particle radius
V	Volume of a measurement region
α	Strike of an incipient joint
β	Dip of an incipient joint
v	Poisson's ratio
σ	Tensile stress in parallel-bond periphery
σ_c	Tensile strength of parallel bond
σ_{sj}	Tensile strength of smooth-joint bond
$\bar{\sigma}$	Average stress measured in a measurement region
τ	Shear stress in parallel-bond periphery

ϕ	Friction angle of parallel bond
μ	Coefficient of particle friction
μ_{sj}	Coefficient of smooth-joint contact
ΔF_n, ΔF_s	Increments of normal and shear forces in parallel bond
ΔM_n, ΔM_s	Increments of components of parallel bond moment
$\Delta\partial_n, \Delta\partial_s$	Increments of normal and shear displacement, respectively
CNL	Constant normal load
DEM	Discrete element method
FJCM	Flat joint contact model
ISRM	International Society for Rock Mechanics and Rock Engineering
LR	Loading rate
PBM	Parallel bond model
PFC	Particle flow code
RFPA	Rock failure process analysis
SJM	Smooth joint model
UCS	Uniaxial compressive strength

1 Introduction

Incipient rock joints retain considerable tensile and shear strength as a result of partial development, which may be due to varying stress conditions, secondary mineralization or cementation processes (Hoek 2007; Hencher 2012; Shang et al. 2016). These incipient rock joints often develop over geological time into full mechanical joints (Hencher 2014), which have zero true cohesion as defined by ISRM (1978).

The term ‘rock bridge’ is defined as a small area of intact/strong rock material separating coplanar or non-coplanar joints in rock masses (Kim et al. 2007), which usually occupy a part of joint place (Dershowitz and Einstein 1988). Fig. 1 shows two surfaces of a broken Horton Formation Siltstone core after direct tension, on which an intact rock bridge was unveiled (red dashed areas in Figs. 1a and 1b). Rock bridges lead to non-persistent nature of rock joints and play a vital role in stabilizing rock masses (e.g. Zheng et al. 2015; Paronuzzi et al. 2016) such as in engineered rock slopes (Hencher 2006).

In rock engineering, failure is often accompanied by the sudden rupture of rock bridges (Paronuzzi et al. 2016), which can be triggered by insolation (Collins and Stock 2016), precipitation (Wieczorek and Jäger 1996), weathering (Borrelli et al. 2007; Hencher 2014; Goudie 2016) and seismic loading (Cravero and Labichino 2004). Gradual initiation, propagation and coalescence of rock bridges within incipient rock joints are likely to be additional challenges confronting practitioners.

Joint persistence is the areal extent of an incipient rock joint (Einstein et al. 1983). The areal persistence definition allows the effects of the incipient parts of a discontinuity (represented by rock bridges) to be taken into account in the stability analysis of rock engineering. Fig. 2 illustrates the terminologies used for the description of an incipient joint plane. The areal persistence, *K*, of this joint plane is expressed by Eq. 1.

$$K = \sum \frac{A_{\mathrm{j}1}+A_{\mathrm{j}2}+\cdots+A_{\mathrm{j}n}}{A_{\mathrm{j}1}+A_{\mathrm{j}2}+\cdots+A_{\mathrm{j}n}+A_{\mathrm{B}}} \quad (1)\ \text{(Lajtai 1969b)}$$

where $A_{\mathrm{j}1}, A_{\mathrm{j}2}, \ldots, A_{\mathrm{j}n}$ are the persistent areas along the joint plane, while A_{B} is the total area of rock bridges.

Previous publications on the shear properties of individual rock discontinuities focused on the mechanical ones with zero true cohesion (e.g. Cawsey and Farrar 1976; Barton 1976; Kulatilake et al. 1999; Karami and Stead 2008; Hencher and

Richards 2015; Ge et al. 2017). For non-filled incipient rock joints, shear strength is mainly controlled by four components, including: fundamental shear strength of rock bridges (Shang et al. 2018a); internal friction in solid bridges (after rock bridge is mobilized); friction from the persistent joint segments (Lajtai 1969b; Maksimović 1996); geometry and location of bridges (Ghazvinian et al. 2007). Rock bridges significantly increase the shear strength of incipient rock joints, since they effectively produce a strength reserve which need to be mobilised prior to failure (Jennings 1970; Stimpson 1978; Gehle and Kutter 2003; Paronuzzi et al. 2016).

It is, however, rare to see laboratory shear testing on natural incipient rock joints as it seems impossible to secure groups of natural rock samples containing discontinuities with identical geometrical characteristics (Shang et al. 2017c). Boulon et al (2002) reported an experimental study of the shear properties of incipient calcite-healed joints that were prepared by sawing blocks containing incipient joints. The sample preparation process was carefully controlled to prevent incipient joint planes from breaking. Similar sample preparation was used by Shang et al (2015 and 2016) to investigate the tensile strength of incipient geological discontinuities. In many studies, artificial samples were used as an alternative to investigate the mechanical properties of rock masses and discontinuities (e.g. Bandis et al. 1981; Grasselli 2006; Hossaini et al. 2014; Liu et al. 2017).

Lagtai (1969a) reported a pioneered work on shear testing of incipient rock joints. One main finding of that work was that shear strength was controlled solely by the tensile strength of solid rock bridges, provided the frictional resistance was negligible. Ghazvinian et al. (2007) presented a laboratory investigation on the effect of rock bridge geometry on the shear properties of planar joints. Plaster block samples having different types of rock bridges were moulded. The study concluded that the failure patterns and shear strength of their samples were controlled by the geometry of rock bridges.

It has to be agreed that rock joints containing rock bridges with different geometrical parameters are readily to be analysed in numerical analysis (e.g. Cundall 2000; Pariseau et al. 2008; Park and Song 2009; Ghazvinian et al. 2012; Huang et al 2015). Zhang et al (2006) reported a 2D numerical direct shear test based on the rock failure process analysis (RFPA) code, in which two edge-notched joints with different linear persistence was investigated. In that study, a dramatic drop of shear strength was observed which was due to the brittle failure of rock bridges. They also found that shear strength of their non-persistent rock joints increased consistently, when the linear persistence value was decreased. A similar two edge-notched numerical model was created by Ghazvinian et al. (2012) using the particle flow code (PFC 2D). Open joints were generated by removing particles. It was found that the progressive failure of tension-induced micro-cracks resulted in the macro-scale shear failure of rock bridges.

In the aforementioned investigations, rock joints are often simplified and treated as linear traces in 2D numerical analysis; these investigations failed to consider the effects of joint geometry and areal persistence on shear characteristics. The present study, therefore, sets out an approach to investigate the effects of areal persistence and geometry of rock bridges on the shear behavior of incipient rock joints. A 3D particle-based model containing incipient rock joints was established based on the Particle Flow Code (PFC 3D). In the particle-based DEM model, rock matrix and bridges were represented as particles that were parallel bonded and persistent joint segments were generated using the smooth-joint model.

2 Numerical model set-up and calibration

2.1 Parallel bond model in PFC3D

In the parallel bond model (PBM), rock matrix is represented by a combination of rigid particles with parallel bond at their contacts (see Fig. 3a), which can transmit both force and moment (Itasca Consulting Group Inc 2008). The mechanism of force and moment of PBM is described by Eqs. 2 to 5.

$$\Delta F_n = k_n A \Delta \partial_n \quad (2)$$

$$\Delta F_s = -k_s A \Delta \partial_s \quad (3)$$

$$\Delta M_n = -k_n J^* \Delta \theta_n \quad (4)$$

$$\Delta M_s = -k_s I \Delta \theta_s \quad (5)$$

where ΔF_n and ΔF_s are increments of normal and shear forces and $F_n>0$ is tension. ΔM_n and ΔM_s are increments of components of parallel-bond moment; k_n and k_s are normal and shear stiffness of the parallel bond; $\Delta\partial_n$ and $\Delta\partial_s$ are increments of normal and shear displacement, respectively; J^* and I are polar moment and moment of inertia of the cross section of parallel bond and A is the cross-sectional area of bond. The tensile and shear strength of the parallel-bond can be calculated using Eqs. 6 and 7. The bond will break if applied stresses exceed the tensile or shear strength of bond, thus failure of rock can be simulated in either tension or shear.

$$\sigma = \frac{F_n}{A} + k\frac{|M_s|R}{I} \quad (6)$$

$$\tau = \frac{F_s}{A} + k\frac{|M_n|R}{J^*} \text{ (3D)} \quad (7)$$

where σ and τ are tensile and shear stresses of the parallel-bond periphery; R is a bond cross-sectional property (shown in Fig. 3a). k is the moment-contribution factor to strength, see Potyondy (2011) for more details.

2.2 Smooth joint model

Bond removal (e.g. Cundall 2000) and bond weakening of particles of a joint plane (e.g. Kulatilake et al. 2001; Huang et al. 2015) are often used as ways of generating rock joints. In those methods, particles laying on one side of joint place will ride over particles on the other side which leads to unrealistic simulation of mechanical behaviour of rock joints due to stress concentration (interlocking) and significant dilation at the initial stage of shearing (Bahaaddini et al. 2013). To overcome this problem, Pierce et al (2007) proposed the smooth joint model (SJM) which allows smooth-jointed particles lie upon opposite sides of joint overlap and slide past each other (see Fig. 3b). The SJM provides linear elastic behaviour of joint interfaces and does not resist relative rotation (Itasca Consulting Group Inc 2008).

It is worthwhile mentioning that the persistent portions of the incipient joints simulated in the current study have zero true cohesion (tensile strength=0). The smooth joint interface in this study was not bonded and there will be no cracks (bond break) between smooth jointed particles.

2.3 Setup of 3D direct shear tests of incipient rock joints

Fig. 4 shows numerical setup of the 3D direct shear tests. Rock samples with length 100 mm, width 100 mm and height 40 mm were produced which consist of around 49000 particles with minimum particle radius R_{min}=1.0 mm and R_{max}/R_{min}=1.5 that follows a uniform distribution (Shang et al. 2017b). For each sample (Fig. 4a), an incipient rock joint with a dip of 0° was generated, represented by the non-persistent joint trace (see the yellow particles in Fig. 4a). Fig. 4b shows the 3D geometry of the persistent portions of the incipient joint (particles of the rock matrix and the rock bridge were not shown for clarity). The rock bridge through the joint plane was embraced by the red dashed lines. In the present study, nineteen incipient rock joints with different geometries (different locations and numbers of rock bridges) were produced, and they were divided into 5 groups (A-E, Fig. 4c)). Areal persistence of these joints varied from 0.2 (A1) to 0.96 (D4). It should be noted that planar incipient rock joints were simulated and focused on in this study, without consideration of roughness and asperities (see Discussion on this simplification).

In the shear test, the lower box was fixed and the upper box was sheared in the positive X-direction (see Fig. 4a) at a constant velocity of 0.02 m/s to ensure quasi-static equilibrium (Park and Song 2009). Samples were sheared under different normal stresses, i.e., 2, 4 and 6 MPa, which was controlled by the servo-mechanism on the top shear box (Itasca Consulting Group Inc 2008). The time-step for each calculation cycle was 1.3333X10^{-7}s.

2.4 Calibration of particle-based DEM

The aim of the calibration of particle-based DEM is to choose suitable input micro-parameters that can reproduce a simulated macroscopic response close to that of the laboratory test results (Kulatilake et al. 2001). The calibration process in this investigation involved the determination of micro-parameters for PBM and SJM, as shown in Table 1.

2.4.1 Calibration of PBM

The DEM model was calibrated against physical experiments of Horton Formation Siltstone, which is typically medium to dark grey strong to extremely strong, formed approximately 421 to 423 million years ago in the Silurian period (Shang 2016). The rock is quarried at Dry Rigg Quarry, Horton-in-Ribblesdale, Settle, north England. Uniaxial compressive test has often been used to calibrate bonded model (e.g. Park and Song 2009; Bahaaddini et al. 2013; Duan and Kwok 2016), thus the PBM model was calibrated against uniaxial compressive strength (UCS), Young's modulus (*E*) and Poisson's ratio (*v*). Table 1 shows the micro-parameters of BPM and the corresponding related macro-parameters. A numerical cylindrical sample containing 9596 particles with a radius ranging between 1.0 and 1.5 mm was generated. The size of the cylindrical DEM sample ($H \times R$ = 120 mm × 50 mm) was same as that used for the laboratory experiment. Calibration process was similar to that used by Bahaaddini et al. (2013) and Shang et al. (2018a), in which Young's modulus, *E*, was firstly calibrated through a trial-and-error process, by adjusting particle linear contact modulus E_c, linear contact normal to shear stiffness ratio K_n/K_s, parallel bond modulus $E_{c\_}$ and parallel bond normal to shear stiffness ratio $K_{n\_}/K_{s\_}$. The Poisson's ratio, *v,* which is controlled by stiffness of both linear contact and bond (see Table 1) was subsequently calibrated. UCS was lastly matched through fine-tuning the cohesion and tensile strength of bond (*c* and σ_c).

Fig. 5a shows a comparison of the results of the calibrated numerical model and laboratory experiment. Failure patterns of real and simulated samples were also included, on which primary fractures were highlighted. It can be seen that numerical results agreed well with the laboratory test results. The corresponding calibrated micro-parameters of BPM are listed in Table 2. Comparison between laboratory test results and those obtained from the calibrated numerical model is shown in Table 3.

2.4.2 Calibration of SJM

The smooth joint parameters were calibrated against direct shear and normal deformability tests on planar and opened joints with zero true cohesion, as used by Kulatilake et al. (2001). Again, micro-parameters (see Table 1) in the numerical model were altered through trial-and-error to match the direct shear and normal deformability test results in the laboratory (see Shang et al. 2018a for details). Figs. 5b, 5c and Table 3 show a comparison between results from laboratory tests and numerical simulations. The results demonstrated that the calibrated SJM can reproduce the direct shear behaviour of the planar Horton Formation Siltstone joint. Table 2 lists the calibrated micro-parameters of SJM. Note that tensile strength and cohesion of the smooth-joint bond were set to zero for the persistent portions of the incipient joints in this study.

3 Numerical results and interpretation

As described earlier, a series of numerical shear tests were conducted on incipient rock joints with 19 different geometrical properties under different normal stresses (2, 4 and 6 MPa). As shown in Fig 4c, samples were divided into five groups, i.e., Groups A-D (rock joints with a single rock bridge) and Group E (rock joints with multiple rock bridges).

3.1 Crack initiation, propagation and coalescence: observations at microscale

3.1.1 Incipient rock joints with a single rock bridge

Microstructure controls micromechanisms occurring in rock, which are complex and difficult to characterize (Potyondy and Cundall 2004). As mentioned earlier, in the particle flow code the bond between cemented particles of rock matrix will break, in either tension or shear, when applied stress equals to or exceeds the strength of cement (bond). Fig. 6 shows an example of crack initiation, propagation and coalescence that were observed in this study (Sample A2; *a*=60 mm, *b*=100 mm, *K*=0.4 and normal stress=6 MPa). Particles of rock matrix and bridge, and parts of walls forming the top shear box are not shown for clarity. As described in Section 2.3, the lower shear box (purple) was fixed and the upper shear box (red) was forced to move with a constant velocity of 0.02 m/s (shown by the red arrow in Fig. 6a). It was observed that cracks were initiated around two edges of the rock bridge (along the X-direction) and these cracks were connected at the cycle of 59436 when shear force was equal to 162.1 kN (Fig. 6b). Shear cracks dominated at this stage (545/603) and note that some scattered cracks were generated within the rock matrix due to stress concentration. More cracks were generated in the middle of the rock bridge at the cycles of 68831 and 72387 (Figs. 6c and 6d) and they propagated dramatically when the shear force rose up to 195.1 kN (Fig. 6e). Peak shear force was observed (211.9 kN) at the cycle of 81795 when cracks coalesced initially in the middle of the rock bridge area (Fig. 6f). The number of shear cracks (5921) at the time of sample failure was around 12 times that of tensile cracks (483). After failure, shear force dropped slightly to 205.3 kN when cracks fully coalesced within the rock bridge area (see Fig. 6g). Fig. 6h shows the final frame of this numerical test when horizontal shear displacement was 1 mm. More tensile cracks (3475) can be seen that was approximately 26.1% that of shear cracks (13319).

For cases with a larger areal persistence (for example Sample D2; *K*=0.88, see Fig. 7), it took shorter time for the shear failure of the incipient rock joints and lesser cracks were induced within the rock bridges.

3.1.2 Incipient rock joints with multiple rock bridges

Numerical results on incipient rock joints with multiple rock bridges (Group E in Fig. 4c) are presented in this section. Fig. 8 shows the crack initiation and propagation of Sample E1 in direct shear test under a normal stress of 4 MPa. Cracks initiated at the cycle of 51200 with a clear concentration on the connection point of two rock bridges (Fig. 8b). The shear force measured at this cycle was 125.5 kN which was 85.4% of the peak shear force (147 kN, Fig. 8h). As shown in Figs. 8c-8g, a steady crack propagation was observed, developing from the middle to the edges of the two rock bridges. The measured peak shear stress of this sample (E1) was 147 kN (Fig. 8h) where the number of shear cracks was 4237, approximately 11 times larger than that of tensile cracks (386). Fig. 8i shows the final frame of the test when horizontal shear displacement was 1.0 mm.

3.2 Shear stress and displacement analysis

It is well accepted that both size and location of rock bridges along a discontinuity will affect its mechanical properties (Zhang et al. 2006; Bonilla-Sierra et al. 2015; Shang et al. 2016). In this study, shear strength of incipient rock joints with different sizes and locations of rock bridges was measured. Fig. 9 shows the relationship between shear stress and horizontal shear displacement of incipient rock joints in Group A (b=100 mm and a=80, 60, 40 and 20 mm, respectively). The cumulative number of cracks (failed in both tension and shear) was tracked and plotted against horizontal displacement (see the dashed lines in Fig. 9). For Sample A1 (see Fig. 9a), the peak shear stress was 24.8 MPa under a normal stress of 6 MPa, and it dropped to 22.1 and 17.5 MPa respectively under lower normal stresses (4 and 2 MPa). Sample A1 failed within a shear displacement of 0.7 mm for the three different normal stresses. A clear yield stage can be seen when normal stress was 2 MPa (black line in Fig. 9a). For all the tested samples in this group, the shear stress and the number of cracks (both tensile and shear cracks) increased with the increase in applied normal stresses. A clear stress drop can be seen at the occurrence of peak shear stress, accompanied with a significant increase of the number of cracks, which can be represented by the sub-vertical slopes of all the dashed curves (see for example Figs. 9c and 9d). These phenomena show some evidence of the brittle property of Horton Formation Siltstone. As anticipated, the number of cracks did not increase when only residual strength left (mainly arising from friction).

Stress and displacement of rock joints in Group B is shown in Fig. 10. Similarly, peak shear strength reduced gradually from B1 to B4 for the same applied normal stress, due to the steady increase of areal persistence (from 0.36 to 0.84). The shear strength of Sample B1 was 21.2 MPa under a normal stress of 6 MPa, which was somewhat smaller than that of Sample A1 (24.8 MPa) in Group A. The yield procedure at a lower normal stress (2 MPa) was also observed (black line in Fig. 10a). The lowest shear strength of the samples in this group was 5.2 MPa (Sample B4 in Fig. 10d) when the applied normal stress was 2 MPa, which was also smaller than that of Sample A4 (6.3 MPa) in Group B (Fig. 9d).

Areal persistence of the samples in Groups C and D were much larger, ranging from 0.72 (C1) to 0.96 (D4). In general, shear strength of the samples in these two groups was smaller than that of those samples in Groups A and B. Similarly, as the normal applied stress increased, the peak shear stress increased (Figs. 11 and 12). Lesser number of cracks was observed compared with that in Groups A and B. The peak shear displacement (shear displacement at peak shear strength) increased with the increment of applied normal stresses which was similar to the findings by Bahaaddini (2013). Fig. 13 presents an example of the relationship between normal displacement and shear displacement observed in the numerical shear tests. It shows that higher normal stress leads to smaller normal displacement.

3.3 Static stress within rock bridges: microscale behaviour

In the particle-based DEM model, the contact force and displacement of particles inside a measurement region can be computed at microscale (Itasca Consulting Group Inc 2008). In static situation, average stress $\bar{\sigma}$ in the measurement region can be expressive in terms of contact forces which is described by Eq. 8.

$$\bar{\sigma} = -\frac{1}{V}\sum_{0}^{N_c} F^c \otimes L^c \qquad (8)$$

where V is the volume of the measurement region; N_c is the number of active contacts within the region; F^c is the vector of each contact force; L^c is a branch vector and the operator $\otimes$ represents outer product.

To investigate the evolution of static stress within rock bridges in the direct shear tests, measurement spheres were distributed in the rock bridge areas. Fig. 14 shows the relationships between stresses measured at different locations and calculation step (Sample B3, normal stress =4 MPa). Eight measurement spheres with the same radius (10 mm) were arranged within the rock bridge area, as shown in the insert diagram in Fig. 14a. For the stresses measured in XX direction (Fig. 14a), stresses measured at different positions showed a similar trend, where a peak shear stress of 28.2 MPa was measured at the step of around 60000. Tensile stress (negative) in the XX direction was measured after the step of 120000, while they were tracked much earlier in YY (Fig. 14b) and XY (Fig. 14c) directions. For the stresses at the ZZ direction, both compressive and tensile stresses were measured before the failure of the sample (around 60000 steps), after which the compressive stress dominated (Fig. 14d).

3.4 Orientation of cracks

Induced cracks in rock may distribute in different directions relying on the combination of mineral grains (Peng et al. 2017), stress distributions (Paterson and Wong 2005) and confinement (Martini et al. 1997). Fig. 15 shows stereonet plots (equal-areal projection) of shear and tensile cracks monitored after simulations C3 (*a*=40 mm and *b*=40 mm, Fig. 4c). Three different loading stresses were applied (2, 4 and 6 MPa). Cracks were plotted as poles and contour lines showing statistical pole concentration were calculated. For comparison, contour interval was set to 2 and legends were indicated in each diagram. The filled contoured areas in Fig. 15a represented densities of 2, 4 and 6% per 1% area for the shear cracks created at a normal stress of 2 MPa, and geometries of these contoured areas changed slightly at different normal stresses (see Figs. 15c and 15e). Densities of tensile cracks ranged between 2, 4 and 6% per 1% area when normal stress was 2 MPa (Fig. 15b), while they were between 2 and 12% per 1% area when normal stress increased to 4 MPa (Fig. 15d) and further increased up to 14 % per 1% area when normal stress was 6 MPa (Fig. 15f).

3.5 Contact force between particles

Fig. 16 shows the distribution of contact forces between particles of rock matrix and joints after shear (Sample C3). Magnitudes, orientations (shown on the XY plane) and the number of active contact forces are presented. It can be seen that contact force between particles (either forming rock matrix or joints), varied with different normal loading conditions. Forces between particles of smooth joints were much smaller than that between particles of rock matrix (parallel bonded).

3.6 Effect of loading rate on shear strength

Shear strength of a rock discontinuity may be influenced by loading velocity (Schneider 1977; Atapour and Moosavi 2014). It is suggested that static shear strength of rock joints should be assessed at a low shearing velocity to ensure an equilibrium status (Muralha et al. 2013). To investigate the effect of loading rate (LR) on the shear properties of incipient rock joints, samples containing single and multiple rock bridges were sheared at different loading rates of 0.01, 0.02, 0.1, 0.5 and 1.0 m/s, respectively. Fig. 17a shows the test results of Sample A2 with a single rock bridge, where stress is plotted against strain (upper part) and the number of cracks created in each loading velocity are also included (lower part). The results show that there was a dramatic increase in shear strength when LR was increased. The peak shear strength was 13.6 MPa of Sample A2 at a LR of 0.01 m/s, while it increased to 17.5 MPa when the LR was 0.1 m/s. It increased further to 18.3 and 21.5 MPa at a LR of 0.5 and 1.0 m/s. Residual strength of the sample was quite close (around 5 MPa), irrespective of LR. The number of tracked cracks increased with the increment of LR. It was 11789 at a LR of 0.01 m/s while it rose up to around 17500 when the LR increased to 1.0 m/s. It was also noted that oscillation of the stress-strain curves can be observed (before failure) if shear velocities were high (0.1, 0.5 and 1.0 m/s in the study). The oscillatory behaviour was eliminated when LR was reduced to 0.02 and 0.01 m/s (see Fig 17a). Furthermore, the difference between the numerical tests (in terms of shear strength and number of cracks) at shearing velocities of 0.02 and 0.01 m/s was insignificant, which means that the loading rate effect is negligible when the shear velocity was reduced to 0.02 m/s.

The measured results of Sample E2 having multiple rock bridges are shown in Fig. 17b. Again, stresses and the number of cracks created in each case are both plotted against horizontal strain. A steady increase in shear strength from 15.1 to 17.5 MPa was observed when LR was increased, similar to the findings shown in Fig. 17a. The total number of cracks were also increased with increase in LR, ranging from 12483 (0.01m/s) to 15520 (1.0 m/s) with a net increment of 24.3%.

3.7 Effect of areal persistence on shear strength

Extensive investigations have been undertaken to study the effect of linear persistence to shear strength of rock discontinuities (for example Lajtai 1969a; Zhang et al. 2006). Shang et al. (2017) has demonstrated the errors in the approximation of areal persistence (real persistence) using linear persistence. Fig. 18 shows the shear stress and shear strain curves of incipient rock joints with different areal persistence ranging from 0.2 to 0.88. It demonstrated that the shear strength reduced from 25.1 to 7.3 MPa when joint areal persistence was increased. Fig. 19 shows that shear strength was also different for samples having the same areal persistence (*K*=0.84) but different geometries of rock bridge. The shear strength of Sample D1 (with a rock bridge area of *a*=80 mm and *b*=20 mm) was the largest (9.2 MPa), and it was 8.3 MPa for Sample B4 having a rock bridge of *a*=20 mm and *b*= 80 mm. The shear strength of Sample C3 with the same area of rock bridge (*a*=40 mm and *b*=40 mm) lay in between.

A further study was conducted on samples of incipient rock joints with multiple rock bridges and same areal persistence (*K*=0.5). The relationship between the shear stress and shear strain of those tested samples is shown in Fig. 20, together with the diagrams of persistent joints (yellow particles). The measured shear strength of

Sample E2 was observed to be the largest, compared with other samples, irrespective of applied normal stresses. Under a lower normal stress (4 MPa), the shear strength was 15.8 MPa for Sample B2, while the shear strengths of Samples E1 and E3 were 14.5 and 13.7 MPa, respectively (solid lines in Fig. 20). The shear strength of Sample E2 increased to 17.9 MPa when the applied normal stress was 6 MPa (red dashed line in Fig. 20), which was somewhat larger than the measured strength of Samples E1 (17.2 MPa) and E3 (16.3 MPa) at the same normal stress.

4 Discussion and limitations of this study

Current definitions of joint areal persistence imply that rock joints are planar in shape (Lajtai 1969b; Jennings 1970; Einstein et al. 1983; Shang et al. 2018b). In this study, planar incipient rock joints having rock bridges with 19 different geometries were produced based on this assumption, which will unavoidably have some limitations as many rock joints observed in the field are non-planar. For example the Woodworth's (1896) observation of joint geometry in Cambridge Argillite (Metamorphosed shale) demonstrated that rock joints are not planar surfaces, but have some distinct surface morphologies. Due to the inaccessible nature of rock masses, information on real joint shape is limited (Zhang and Einstein 2010), although some attempts have been made (e.g. Shang et al. 2017a). For simplicity, planar rock joints have often been used for the investigation of mechanical behaviour of rock masses (e.g. Kemeny 2005; Ghazvinian 2007; Yang et al. 2016; Liu et al. 2017), including the present paper. Additionally, as mentioned in DEM model setup (Section 2.3), persistent sections (planar and opened joint sections) of the planar incipient rock joints were simulated in this study without consideration of roughness and asperities. The main reason for this simplification is restricted by the scope of this study, which aims at investigating the effects of spatial distribution of rock bridges and areal persistence on the shear characteristics of planar incipient rock joints. The contribution to shear strength of an incipient rock joint from intact rock bridges can be much larger than that from the small asperities of a planar and opened joint plane (Gehle and Kutter 2003). For example, shear strength of the intact Horton Formation Siltstone in this study (around 17.5 MPa, see Fig. 9a, black line) was approximately 10 times larger than that of a planar and opened joint (1.54 MPa, see Fig 5c). This simplification therefore, has little effects on the shear strength of the planar incipient rock joints focused in the study.

Fracturing and rupture of a piece of intact rock are influenced by mineralogy (Bieniawski 1967), which is complex and inhomogeneous. Cracks preferentially initiate along mineral grain boundaries between neighbouring hard minerals (e.g. quartz) and soft minerals (e.g. K-feldspar) and sometimes occur within mineral grains as applied stress increases (Eberhardt et al. 1999), which are often called intergranular failure and transgranular failure, respectively. The particle-based DEM established in this study did not attempt to simulate specific mineralogical grains but represented rock as an assembly of grains (which is a common practice in the PFC) that can exhibit macro-mechanical behaviour of the simulated rock. Rock bridges ruptured suddenly after the initiation of cracks accompanied with a dramatic increase in the number of cracks (Figs. 9-12), especially when the number of rock bridges increased (see Fig. 8). This finding agrees with the brittle rupture of the Horton Formation Siltstone observed in the laboratory and in the field (Shang et al 2016). The induced cracks orientated with much more concentration under higher normal stresses (Fig. 15).

It has been found that the number of shear cracks (at microscale) was approximately 10 times more than that of tensile cracks after shear failure (Fig. 6-8). The smaller number of tensile cracks observed in the study can be attributed to (1) the nature of the tests reported in the study, where DEM samples were failed in pure mode II shear pattern from a macroscopic point of view, which can lead to more shear cracks; and (2) the intrinsic limitation of the standard PBM which overestimates the tensile strength of rock used in the study (especially when uniaxial compressive tests are used in model calibration). As described in Section 2.4.1, uniaxial compressive tests were used to calibrate the PBM, following the procedures used by Bahaaddini et al (2013) and Shang et al. (2018a). In the calibration process, parallel bond microparameters were properly selected to match UCS of Horton Formation Siltstone (see Fig. 5a), which has inevitably led to the overestimation of tensile strength of the rock. This fact is due to the use of spherical grains in the standard PBM which cannot provide adequate grain interlocking (after the parallel bond is broken and vanished) as that of real rocks (Potyondy and Cundall 2004). To eliminate this intrinsic limitation of the standard PBM, the flat joint contact model (FJCM) proposed by Potyondy (2012) is suggested to be used in future research. In the FJCM, the interfaces between cemented particles can be damaged partially and still exist after bond breakage which can provide much more interlocking between particles (Potyondy 2012). Potyondy (2013) and Vallejos et al. (2017) have demonstrated that the calculated compressive-to-tensile strength ratio based on the FJCM is able to match that of experimental results.

Strength of rock joints is closely related to joint persistence. Many numerical researches have been conducted on this topic (e.g. Zhang et al. 2006; Prudencio and Van Sint Jan 2007; Jiang et al. 2015). However in most of the previous studies, linear persistence was used as a way of representing real joint persistence, which will unavoidably have some limitations and even errors, as pointed out by Zhang and

Einstein (2010), and Shang et al. (2017a). In this paper, the relationship between joint areal persistence and shear strength was investigated. Results demonstrated that shear strength increased gradually with decrease in areal persistence (Fig. 18), which agrees with the findings by Zhang et al. (2006). Moreover, Figs. 19 and 20 revealed that shear strength can also be different for incipient rock joints with the same areal persistence.

5 Summary and conclusions

Fifty-seven direct shear tests under constant normal load boundary conditions have been conducted on planar incipient rock joints using the established 3D particle-based DEM model, in which rock bridges with nineteen different geometries were involved. The DEM model was calibrated against physical experiments of Horton Formation Siltstone. Shear behaviour of incipient rock joints with various geometries of rock bridges was then investigated. It is demonstrated that the established 3D particle-based DEM model can reproduce the shear behaviour and micromechanical properties of incipient rock joints with various geometries of rock bridges within the Horton Formation Siltstone. The following conclusions are made from this study:

(1) Based on the calibrated 3D particle-based DEM model, cracks often initiated at the edges of rock bridges in direct shear. For cases with a single rock bridge, cracks propagated and coalesced initially in the middle of rock bridge areas; while for cases with multiple rock bridges, cracks firstly concentrated around the connection points of rock bridges and then propagated until sample failure

(2) Rock bridge portions of tested incipient rock joints exhibited a quite brittle failure under direct shear, accompanied with a dramatic increase of the number of cracks. Shear cracks dominated for all tests in the study and this may be due to the nature of

the mode II tests reported in the study and the intrinsic limitation of the standard PBM which overestimates tensile strength of rock used in the study. High crack initiation stresses were measured (more than 60% of shear strength) for all tested rock joints and they varied with rock bridge geometries.

(3) Shear strength of incipient rock joints tested in the study increased when the applied normal stress was increased. Areal persistence played a significant role in the shear strength of incipient rock joints. Shear strength increased gradually when joint areal persistence was decreased. The number and distribution of rock bridges on the joint planes also affected the shear strength of incipient rock joints. For some rock joints with the same areal persistence (e.g. K=0.5), the measured shear strength was still different.

(4) The shearing velocity also affected shear strength, irrespective of the number of rock bridges. It was found that a high shearing velocity (1.0 m/s) resulted in a higher shear strength, and simultaneously a strong oscillation of stress-strain curves can be observed. To eliminate the shearing velocity effect, in the study, a shearing velocity of 0.02 m/s was used.

It has to be noted that in the current research rock bridges with a regular geometry (rectangular) were simulated. This of course implies a simplified description of the geometry of natural rock bridges. An ongoing work is attempting to study the statistical distribution (fractal) and geometry of real rock bridges based on laboratory and field observations, which will be an extension of the current study.

Acknowledgement

The research was partially funded by the National Natural Science Foundation of China: Mechanism and test of time-varying and multi-scale behaviours of rock mass under deep mining (No. 41672298). The stereonet developed by Prof. Richard Allmendinger of Cornell University was used to interpret orientations of cracks. The editor-in-chief Prof. Giovanni Barla and the two anonymous reviewers are thanked for their valuable comments.

References

Atapour H, Moosavi M (2014) The influence of shearing velocity on shear behaviour of artificial joints. Rock Mech Rock Eng 47(5): 1745-1761

Bahaaddini M, Sharrock G, Hebblewhite BK (2013) Numerical direct shear tests to model the shear behaviour of rock joints. Comput Geotech 51: 101-115

Bandis S, Lumsden AC, Barton NR (1981) Experimental studies of scale effects on the shear behaviour of rock joints. Int J Rock Mech Min Sci Geomech Abstr 18(1): 1-21

Barton N (1976) The shear strength of rock and rock joints. Int J Rock Mech Min Sci 13(9): 255-279

Bieniawski ZT (1967) Mechanism of brittle rock fracture: Part I-theory of the fracture process. Int J Rock Mech Min Sci Geomech Abstr 4(4): 395-404, IN11-IN12, 405-406

Bonilla-Sierra V, Scholtès L, Donzé FV, Elmouttie M (2015) DEM analysis of rock bridges and the contribution to rock slope stability in the case of translational sliding failures. Int J Rock Mech Min Sci 80: 67-78

Borrelli L, Greco R, Gullà G (2007) Weathering grade of rock masses as a predisposing factor to slope instabilities: Reconnaissance and control procedures. Geomorphology 87(3): 158-175

Boulon M, Armand G, Hoteit N, Divoux P (2002) Experimental investigations and modelling of shearing of calcite healed discontinuities of granodiorite under typical stresses. Eng Geol 64(2-3): 117-133

Cawsey DC; Farrar NS (1976) A simple sliding apparatus for the measurement of rock joint friction. Geotechnique 26(2): 382-386

Cho N, Matrin CD, Sego DC (2007) A clumped particle model for rock. Int J Rock Mech Min Sci 44(7): 997-1010

Collins BD, Stock GM (2016) Rockfall triggering by cylic thermal stressing of exfoliation fractures. Nat Geosci 9: 395-400

Cravero M, Labichino G (2004) Analysis of the flexural failure of an overhanging rock slab. Int J Rock Mech Min Sci 41(S1): 605-610

Cundall PA (2000) Numerical experiments on rough joints in shear using a bonded particle model. In: Aspects of tectonic faulting, Berlin, pp 1-9

Dershowitz WS, Einstein HH (1988) Characterizing rock joint geometry with joint system models. Rock Mech Rock Eng 21(1): 21-51

Duan K, Kowk CY (2016) Evolution of stress-induced borehole breakout in inherently anisotropic rock: Insights from discrete element modelling. J Geophys Res Solid Earth 121(4): 2361-2381

Eberhardt E, Stimpson B, Stead D (1999) The influence of mineralogy on the initiation of microfractures in granite. In: Proceeding of 9th International Congress on Rock Mechanics, Paris. A.A. Balkema, Rotterdam, pp 1007-1010

Einstein HH, Veneziano D, Baecher GB, Oreilly KJ (1983) The effect of discontinuity persistence on rock slope stability. Int J Rock Mech Min Sci Geomech Abstr 20(5): 227-236

Ge YF, Tang HM, Ez Eldin MAM, Wang LQ, Wu Q, Xiong CR (2017) Evolution process of natural rock joint roughness during direct shear tests. Int J Geomech, doi: 10.1061/(ASCE)GM.1943-5622.0000694

Gehle C, Kutter HK (2003) Breakage and shear behaviour of intermittent rock joints. Int J Rock Mech Min Sci 40(5): 687-700

Ghazvinian A, Nikudel MR, Sarfarazi V (2007) Effect of rock bridge continuity and area on shear behaviour of joints. In: 11th Congress of the International Society for Rock Mechanics, Lisbon, Portugal, pp 247-250

Ghazvinian A, Sarfarzai V, Schubert W, Blumel M (2012) A study of the failure mechanism of planar non-persistenct open joints using PFC2D. Rock Mech Rock Eng 45(5): 677-693

Goudie AS (2016) Quantification of rock control in geomorphology. Earth-Sci Rev 159: 374-387

Grasselli G (2006) Shear strength of rock joints based on quantified surface description. Rock Mech Rock Eng 39(4): 295-314

Hencher SR (2006) Weathering and erosion process in rock - implications for geotechnical engineering. In: Proceedings symposium on Hong Kong soils and rocks, Centre for research and progessional development, IMMM, Geological Society, HKRG, Hong Kong, pp 29-79.

Hencher SR (2012) Practical engineering geology. Spon Press, Taylor & Francis, Oxon, p 467

Hencher SR (2014) Characterizing discontinuities in naturally fractured outcrop analogues and rock core: the need to consider fracture development over geological time. Advances in the study of fractured reservoirs. Geol Soc London Spec Publ 374: 113-123

Hencher SR, Richards LR (2015) Assessing the shearing strength of rock discontinuities at laboratory and field scales. Rock Mech Rock Eng 48: 883-905

Hoek E (2007) Practical rock engineering. Hoek's corner, p 342. http://www.rocscience.com

Hossaini KA, Babanouri N, Nasab SK (2015) The influence of asperity deformability on the mechanical behaviour of rock joints. Int J Rock Mech Min Sci 70: 154-161

Huang D, Cen DF, Ma GW, Huang RQ (2015) Step-path failure of rock slopes with intermittent joints. Landslides 12(5): 911-926

ISRM (1978) Suggested methods for the quantitative description of discontinuities in rock masses. Int J Rock Mech Min Sci 15(6): 319-368

Itasca Consulting Group Inc (2008) PFC3D manual, version 4.0. Minneapolis, Minnesota

Jennings JE (1970) A mathematical theory for the calculation of the stability of slopes in open cast mines: Planning Open Pit Mines. In: Proceedings of the Symposium on the Theoretical Background to the Planning of Open Pit Mines with Special Reference to Slope Stability, Johannesburg, pp 87-102

Jiang MJ, Jiang T, Crosta GB, Shi ZM, Chen H, Zhang N (2015) Modelling failure of jointed rock slope with two main joint sets using a novel DEM bond contact model. Eng Geol 193: 79-96.

Karami A, Stead D (2008) Asperity degradation and damage in the direct shear test: A hybrid FEM/DEM approach. Rock Mech Rock Eng 41(2): 229-266

Kemeny J (2005) Time-dependent drift degradation due to the progressive failure of rock bridges along discontinuities. Int J Rock Mech Min Sci 42(1): 35-46

Kim BH, Kaiser PK, Grasselli G (2007) Influence of persistence on behaviour of fractured rock masses. Geol Soc London Spec Publ 284: 161-173

Kulatilake PHSW, Malama B, Wang J (2001) Physical and particle flow modeling of jointed rock block behavior under uniaxial loading. Int J Rock Mech Min Sci 38(5): 641-657

Kulatilake PHSW, Um J, Panda BB, Nghiem N (1999) Development of new peak shear-strength criterion for anisotropic rock joints. J Eng Mech 125(9): 1010-1017

Lajtai EZ (1969a) Strength of discontinuous rocks in direct shear. Geotechnique 19(2): 218-233

Lajtai EZ (1969b) Shear strength of weakness planes in rock. Int J Rock Mech Min Sci 6(5): 499-508, IN7-IN8, 509-515

Liu Y, Dai F, Fan PX, Xu NW, Dong Lu (2017) Experimental investigation of the influence of joint geometric configurations on the mechanical properties of intermittent jointed rock models under cyclic uniaxial compression. Rock Mech Rock Eng 50(6): 1453-1471

Maksimović M (1996) The shear strength components of a rough rock joint. Int J Rock Mech Min Sci Geoch Abstract 33(8): 769-783

Martini CD, Read RS, Martino JB (1997) Observations of brittle failure around a circular test tunnel. Int J Rock Mech Min Sci 34(7): 1065-1073

Muralha J, Grasselli G, Tatone B, Blümel M, Chryssanthakis P, Jiang YJ (2013) ISRM suggested method for laboratory determination of the shear strength of rock joints: revised version. Rock Mech Rock Eng 47(1):291–302

Pariseau WG, Puri S, Schmelter SC (2008) A new model for effects of impersistent joint sets on rock slope stability. Int J Rock Mech Min Sci 45(2): 122-131

Paronuzzi P, Bolla A, Rigo E (2016) 3D stress-strain analysis of a failed limestone wedge influenced by an intact rock bridge. Rock Mech Rock Eng 49(8): 3223-3242

Park JW, Song JJ (2009) Numerical simulation of a direct shear test on a rock joint using a bounded-particle model. Int J Rock Mech Min Sci 46(8): 1315-1328

Paterson MS, Wong TF (2005) Experimental rock deformation – the brittle field (2nd ed.), Springer Berlin, New York, p 348

Pierce M, Cundall P, Potyondy D, Mas Ivars D (2007) A synthetic rock mass model for jointed rock. In: 1st Canada-U.S. Rock Mechanics Symposium, Vancouver, pp 341-349

Potyondy DO (2011) Parallel-Bond Refinements to Match Macroproperties of Hard Rock. In: Continuum and Distinct Element Numerical Modeling in Geomechanics.

Potyondy DO (2012) A flat-jointed bonded-particle material for hard rock. In: Proceeding of 46th US Rock Mechanics/Geomechanics Symposium, American Rock Mechanics Association, Alexandria, VA, pp 1510-1519

Potyondy DO (2013) PFC 3D flat joint contact model version 1, Itasca Consulting Group.

Potyondy DO, Cundall PA (2004) A bonded-particle model for rock. Int J Rock Mech Min Sci 41(8): 1329-1364

Proceedings of Second International FLAC/DEM Symposium, Melbourne, Australia, pp 459-465

Prudencio M, Van Sint Jan M (2007) Strength and failure modes of rock mass models with non-persistent joints. Int J Rock Mech Min Sci 44(6): 890-902

Schneider H (1977) The time dependence of friction of rock joints. Bulletin IAEG 16(1):235–239

Shang J, Hencher SR, West LJ (2015) Tensile strength of incipient rock discontinuities, In: Proceedings of the ISRM regional symposium Eurock 2015 & 64th Geomechanics Colloquium, Salzburg, Austria, pp 565-570

Shang J (2016) Persistence and tensile strength of incipient rock discontinuities. PhD thesis, University of Leeds. Leeds, United Kingdom, p 248

Shang J, Hencher SR, West LJ (2016) Tensile strength of geological discontinuities including incipient bedding, rock joints and mineral veins. Rock Mech Rock Eng 49(11): 4213-4225

Shang J, Hencher SR, West LJ, Handley K (2017a) Forensic excavation of rock masses: A technique to investigate discontinuity persistence. Rock Mech Rock Eng 50(11): 2911-2928

Shang J, Duan K, Gui Y, Handley K, Zhao Z (2017b) Numerical investigation of the direct tensile behaviour of laminated and transversely isotropic rocks containing incipient bedding planes with different strengths. Comput Geotech, https://doi.org/10.1016/j.compgeo.2017.11.007

Shang J, West LJ, Hencher SR, Zhao Z (2017c) Tensile strength of large-scale incipient rock joints: a laboratory investigation. Acta Geotech, https://doi.org/10.1007/s11440-017-0620-7

Shang J, Zhao Z, Ma S (2018a) On the shear failure of incipient rock discontinuities under CNL and CNS boundary conditions: Insights from DEM modelling. Eng Geol 234:153-166

Shang J, West LJ, Hencher SR, Zhao Z (2018b) Geological discontinuity persistence: Implications and quantification. Eng Geol 241: 41-54

Stimpson B (1978) Failure of slopes containing discontinuous planar joints. In: Proceedings of the 19th US Symposium on Rock Mechanics, Stateline, Nevada, pp 296-302

Vallejos JA, Salinas JM, Delonca A, Ivars DM (2017) Calibration and verification of two bonded-particle models for simulation of intact rock behaviour. Int J Geomech, https://doi.org/10.1061/(ASCE)GM.1943-5622.0000773

Wieczorek GF, Jäger S (1996) Triggering mechanisms and depositional rates of postglacial slope-movement processes in the Yosemite Valley, California. Geomorphology 15: 17-31

Woodworth JB (1896) On the fracture system of joints, with remarks on certain great fractures. Boston Soc Nat Hist Proc 27(1): 63–184

Yang XX, Kulatilake PHSW, Chen X, Jing HW, Yang SQ (2016) Particle flow modelling of rock blocks with nonpersistent open joints under uniaxial compression. Int J Geomech 16(6): 04016020, doi: 10.1061/(ASCE)GM.1943-5622.0000649

Zhang HQ, Zhao ZY, Tang CA, Song L (2006) Numerical study of shear behaviour of intermittent rock joints with different geometrical parameters. Int J Rock Mech Min Sci 43(5): 802-816

Zhang LY, Einstein HH (2010) The planar shape of rock joints. Rock Mech Rock Eng 43(1): 55-68

Zheng Y, Xia L, Yu Q (2015) Analysis of the removability and stability of rock blocks by considering the rock bridge effect. Can Geotech J 53(3): 384-395

Figure Captions:

Fig. 1 a and **b** A rock bridge unveiled after the direct tensile failure of a Horton Formation Siltstone. After Shang et al. 2016

Fig. 2 Descriptive terminology for a plane of weakness (an incipient joint). Adapted from Lajtai 1969.

Fig. 3 a Parallel bond model (after Cho et al. 2007) and **b** smooth joint model in PFC.

Fig. 4 Numerical model setup of direct shear tests. **a** A bonded particle model containing a horizontal incipient rock joint; **b** Joint segments (yellow particles) shown in **a** and a rock bridge (embraced by red dashed lines) along the joint plane; **c** Incipient joint planes with a single rock bridge (Groups A-D) and multiple rock bridges (Group E). For more details, see text. Please see the web version of this article for colour interpretation.

Fig. 5 Comparison between results of laboratory experiments and the calibrated DEM model. **a** Unconfined compressive of intact Horton Formation Siltstone. Failure patterns of a DEM sample and a Horton formation Siltstone core are included. Green and red discs in the broken DEM sample represent tensile and shear cracks, respectively; **b** Normal deformability test results and **c** stress against horizontal displacement in the direct shear tests: Numerical modeling results (solid lines) and experimental results (scattered dots). Normal stresses applied were 2, 4 and 6 MPa, respectively.

Fig. 6 Crack initiation, propagation and coalescence of an incipient joint with an areal persistence of 0.4 (*a*=60 mm and *b*=100 mm) within the Sample A2 under direct shear. **a** Test initiation; **b** Crack initiation; **c**-**e** Crack propagation; **f** Crack coalescence; **g** Fully rupture of the rock bridge and **h** final frame of the shear test. Particles of rock matrix and rock bridge and parts of shear box walls are not shown for clarity.

Fig. 7 Crack initiation, propagation and coalescence of an incipient joint with an areal persistence of 0.88 (*a*=60 mm and *b*=20 mm) within the Sample D2 under direct shear. **a** Test initiation; **b** Crack initiation; **c**-**e** Crack propagation and coalescence; **f** Peak shear force reached; **g** Fully rupture of rock bridge and **h** final frame of the shear test.

Fig. 8 Crack initiation, propagation and coalescence of an incipient joint (*K*=0.5) with two rock bridges within the Sample E1 under direct shear. **a** Test initiation; **b** Crack initiation; **c**-**g** Crack propagation and coalescence; **h** Peak shear force reached and **i** final frame of the shear test.

Fig. 9 Shear stress and number of cracks plotted against horizontal displacement of the incipient rock joints in the Group A. **a** A1 with a rock bridge of *a*=100 mm and *b*=80 mm (*K*=0.2); **b** A2 with a rock bridge of *a*=100 mm and *b*=60 mm (*K*=0.4); **c** A3 with a rock bridge of *a*=100 mm and *b*=40 mm (*K*=0.6) and **d** A4 with a rock bridge of *a*=100 mm and *b*=20 mm (*K*=0.8).

Fig. 10 Shear stress and number of cracks plotted against horizontal displacement of samples in the Group B. **a** B1 with a rock bridge of *a*=80 mm and *b*=80 mm (*K*=0.36); **b** B2 with a rock bridge of *a*=800 mm and *b*=60 mm (*K*=0.52); **c** B3 with a rock bridge of *a*=80 mm and *b*=40 mm (*K*=0.68) and **d** B4 with a rock bridge of *a*=80 mm and *b*=20 mm (*K*=0.84).

Fig. 11 Shear stress and number of cracks plotted against horizontal displacement of samples in the Group C. **a** C1 with a rock bridge of *a*=80 mm and *b*=40 mm (*K*=0.72); **b** C2 with a rock bridge of *a*=60 mm and *b*=40 mm (*K*=0.76); **c** C3 with a rock bridge of *a*=40 mm and *b*=40 mm (*K*=0.82) and **d** C4 with a rock bridge of *a*=20 mm and *b*=20 mm (*K*=0.92).

Fig. 12 Shear stress and number of cracks plotted against horizontal displacement of samples in the Group D. **a** D1 with a rock bridge of *a*=80 mm and *b*=20 mm (*K*=0.84); **b** D2 with a rock bridge of *a*=60 mm and *b*=20 mm (*K*=0.88); **c** D3 with a rock bridge of *a*=40 mm and *b*=20 mm (*K*=0.92) and **d** D4 with a rock bridge of *a*=20 mm and *b*=20 mm (*K*=0.96).

Fig. 13 Normal displacement against horizontal shear displacement under normal stresses of 2, 4 and 6 MPa (*a*=80 mm, *b*=40 mm, and *K*=0.68).

Fig. 14 Measured stresses plotted against step. **a** Stress XX; **b** Stress YY; **c** Stress XY and **d** stress ZZ. Eight measurement spheres (shown in **a**) with the same radius of 10 mm were arranged within the rock bridge area. The applied normal stress was 4 MPa (*a*=40 mm, *b*=80 mm, and *K*=0.68).

Fig. 15 Contoured (percent of 1% area) stereonet plots of tensile and shear cracks of an incipient rock joint with a single rock bridge after shear. Normal stresses were 2 (**a** and **b**), 4 (**c** and **d**) and 6 MPa (**e** and **f**), respectively. The different colours stand for contoured data density with different intervals shown in the legend (*a*=40 mm, *b*=40 and *K*=0.84).

Fig. 16 Contact forces between particles of rock matrix and smooth joint of the Sample C3 (*a*=40 mm and *b*=40 mm) after direct shear. Normal stresses were 2 (**a**), 4 (**b**) and 6 MPa (**c**), respectively.

Fig. 17 Shear stress against shear strain at different shearing velocities of 0.02, 0.1, 0.5 and 1.0 m/s (upper part). The number of cracks created were also plotted (lower part). **a** Sample A2 with a single rock bridge (K=0.4) and **b** Sample E2 with multiple rock bridges (K=0.5). Normal stress applied was 4 MPa.

Fig. 18 Shear stress and strain of incipient rock joints with different areal persistence.

Fig. 19 Shear stress and strain relationship of rock joints (within Samples B4, C3 and D1) with the same areal persistence of 0.82. Normal stress was 6 MPa.

Fig. 20 Shear stress and strain relationship of rock joints (in Group E) with the same areal persistence of 0.5.

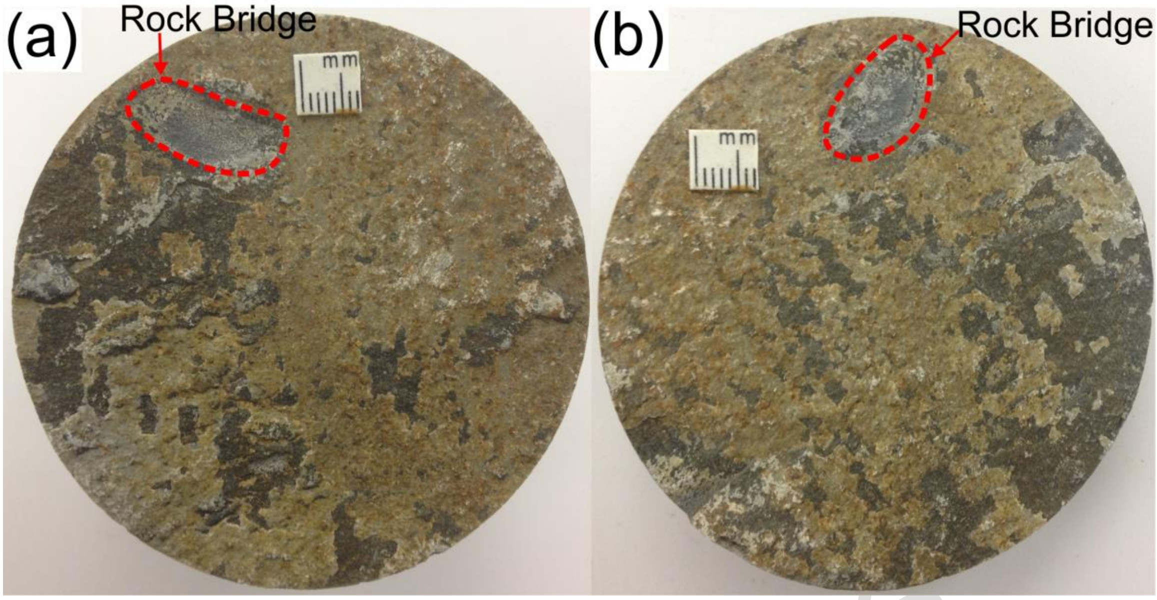

Fig 1

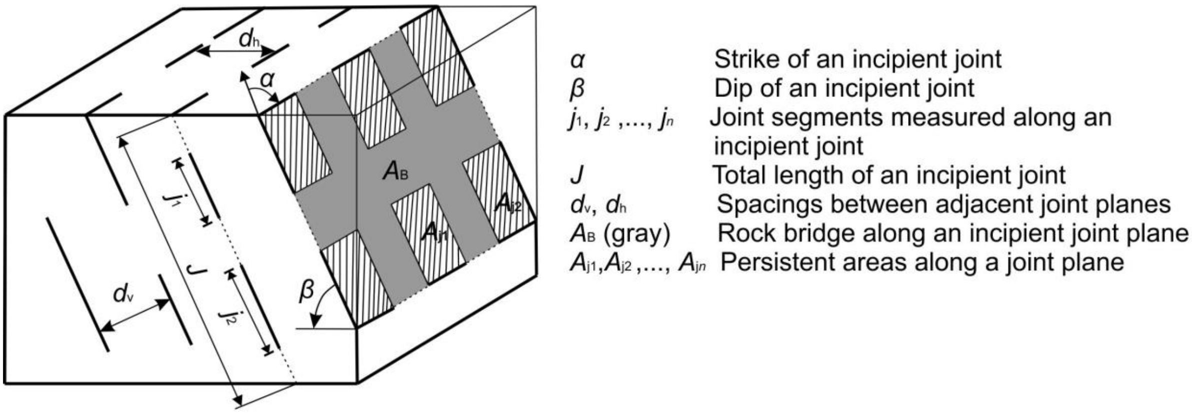

dh
α
AB
Aj1
Aj2
j1
J
j2
dv
β
α Strike of an incipient joint
β Dip of an incipient joint
j1, j2 ,..., jn Joint segments measured along an incipient joint
J Total length of an incipient joint
dv, dh Spacings between adjacent joint planes
AB (gray) Rock bridge along an incipient joint plane
Aj1,Aj2 ,..., Ajn Persistent areas along a joint plane

Fig 2

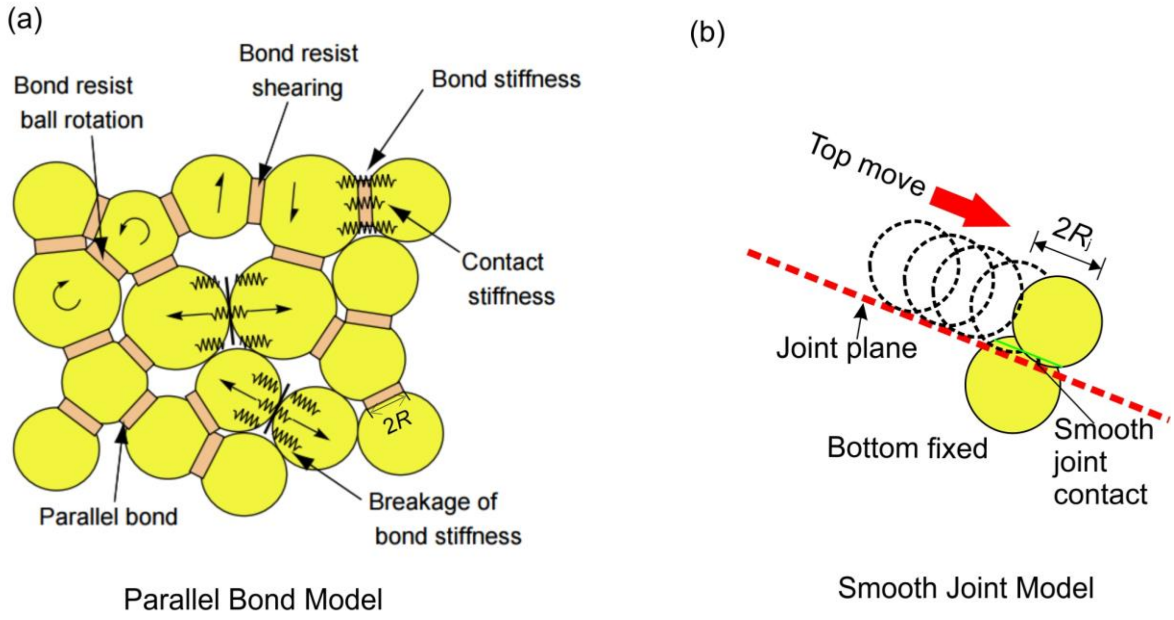
(a)
Bond resist ball rotation
Bond resist shearing
Bond stiffness
Contact stiffness
2R
Parallel bond
Breakage of bond stiffness
Parallel Bond Model
(b)
Top move
2R
Joint plane
Bottom fixed
Smooth joint contact
Smooth Joint Model

Fig 3

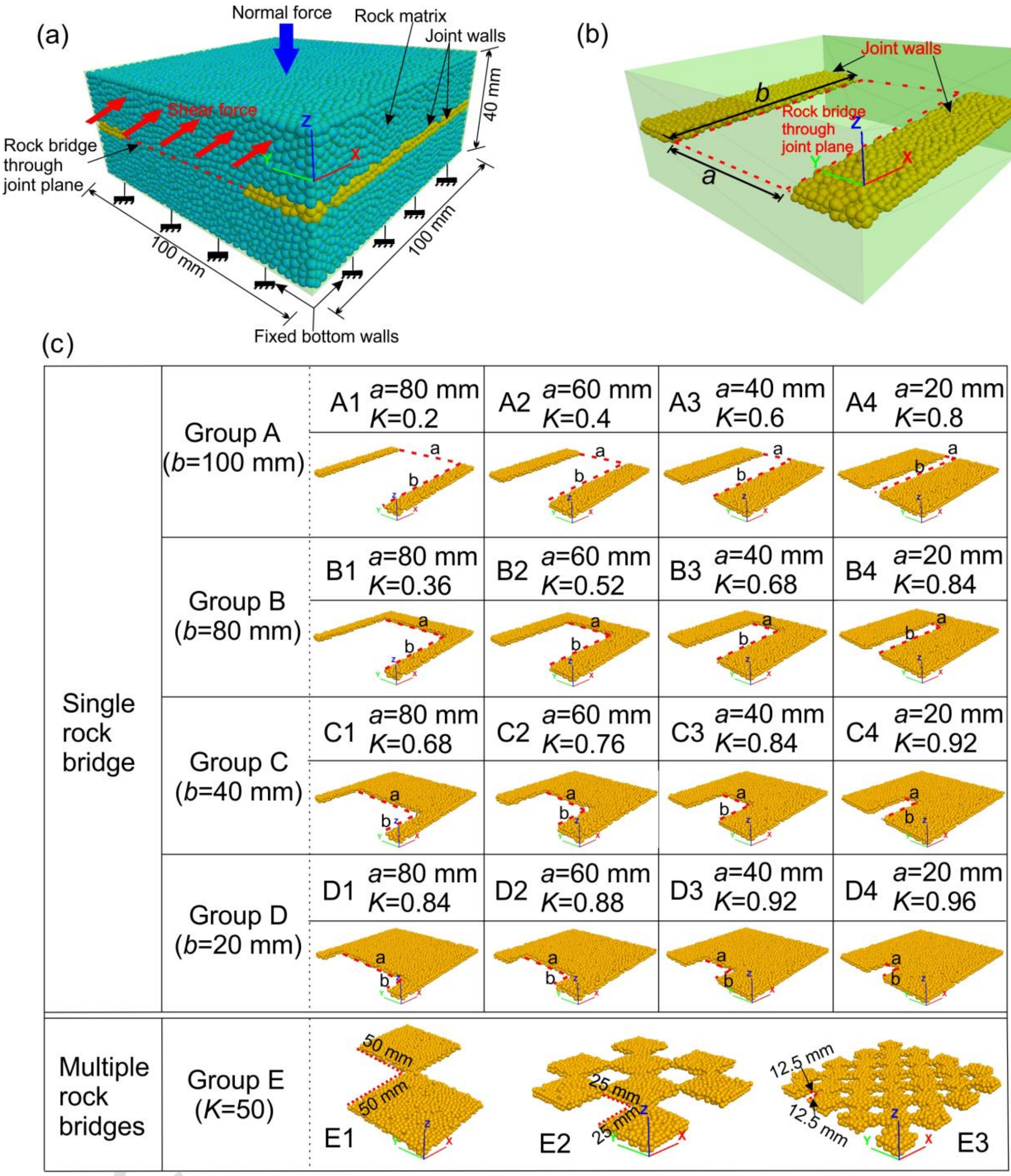

(a)
Normal force
Rock matrix
Joint walls
Shear force
40 mm
Rock bridge through joint plane
Z
Y
X
100 mm
100 mm
Fixed bottom walls
(b)
Joint walls
b
Rock bridge through joint plane
a
(c)
Single rock bridge
Group A (b=100 mm)
A1 a=80 mm K=0.2
A2 a=60 mm K=0.4
A3 a=40 mm K=0.6
A4 a=20 mm K=0.8
Group B (b=80 mm)
B1 a=80 mm K=0.36
B2 a=60 mm K=0.52
B3 a=40 mm K=0.68
B4 a=20 mm K=0.84
Group C (b=40 mm)
C1 a=80 mm K=0.68
C2 a=60 mm K=0.76
C3 a=40 mm K=0.84
C4 a=20 mm K=0.92
Group D (b=20 mm)
D1 a=80 mm K=0.84
D2 a=60 mm K=0.88
D3 a=40 mm K=0.92
D4 a=20 mm K=0.96
Multiple rock bridges
Group E (K=50)
50 mm
50 mm
E1
25 mm
25 mm
E2
12.5 mm
12.5 mm
E3

Fig 4

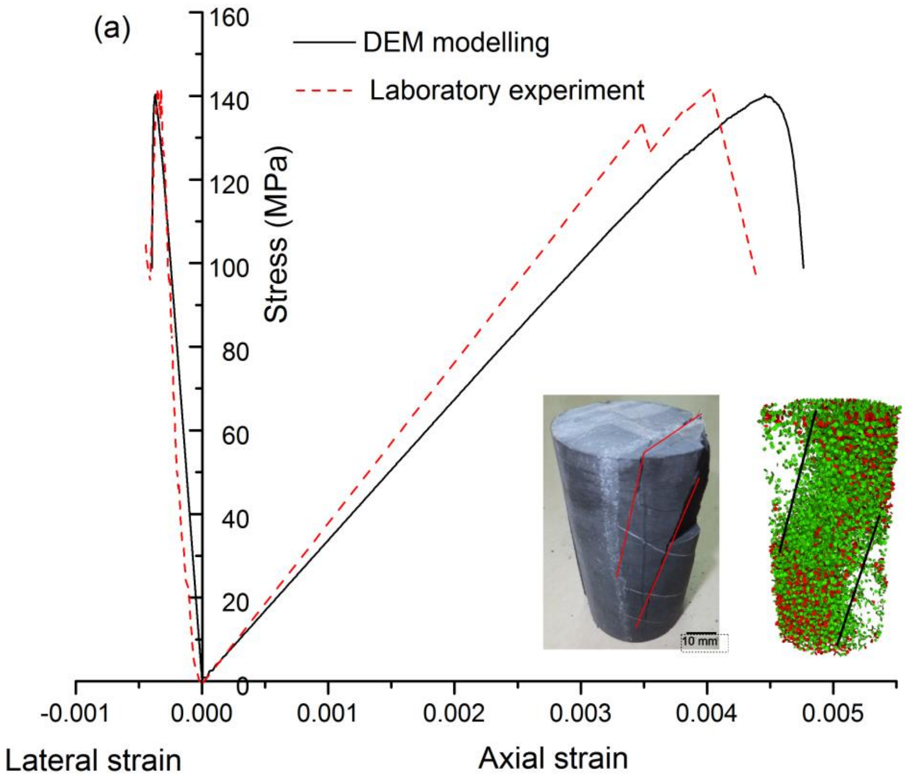

900

901 **Fig 5a**

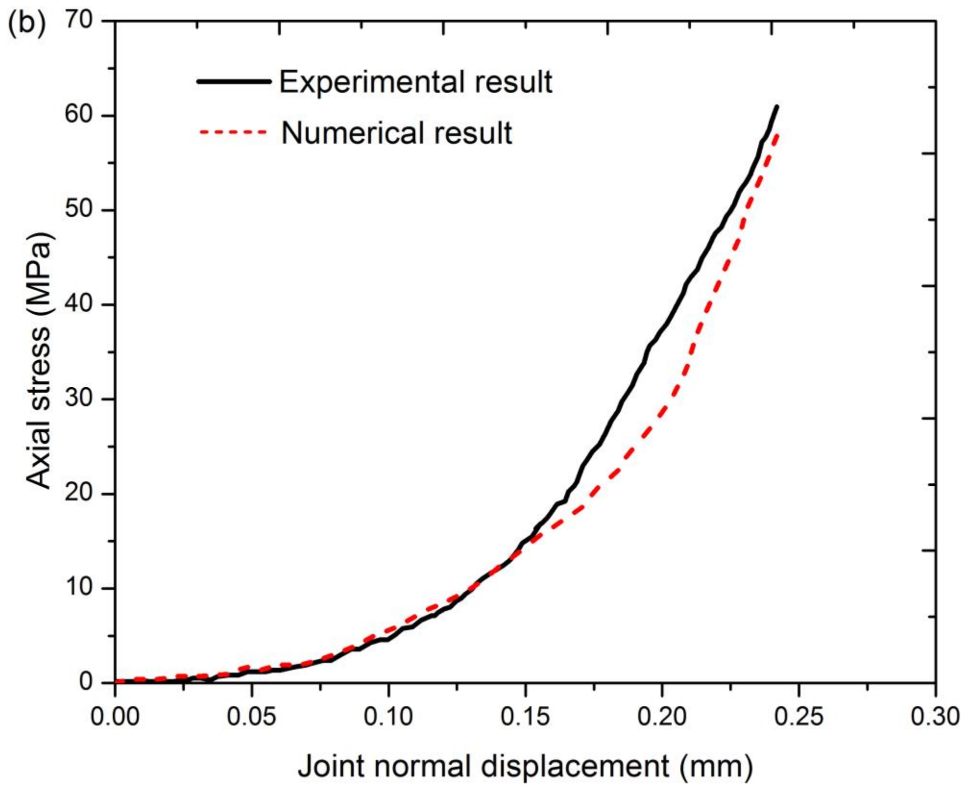
(b)
Experimental result
Numerical result
Axial stress (MPa)
0
10
20
30
40
50
60
70
0.00
0.05
0.10
0.15
0.20
0.25
0.30
Joint normal displacement (mm)

Fig 5b

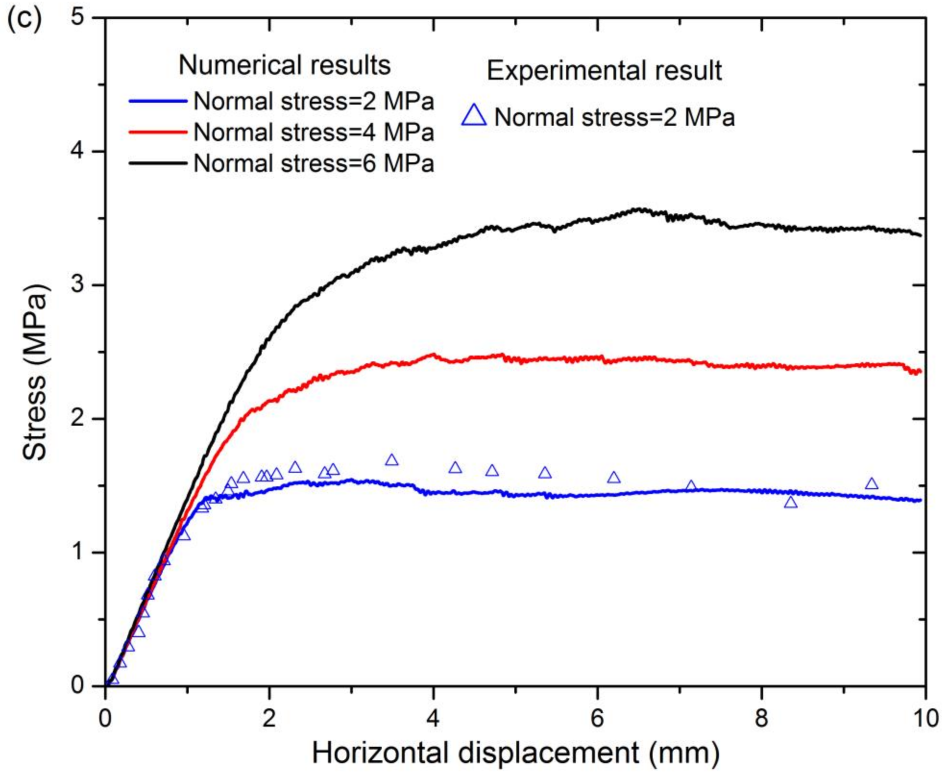

905

906 **Fig 5c**

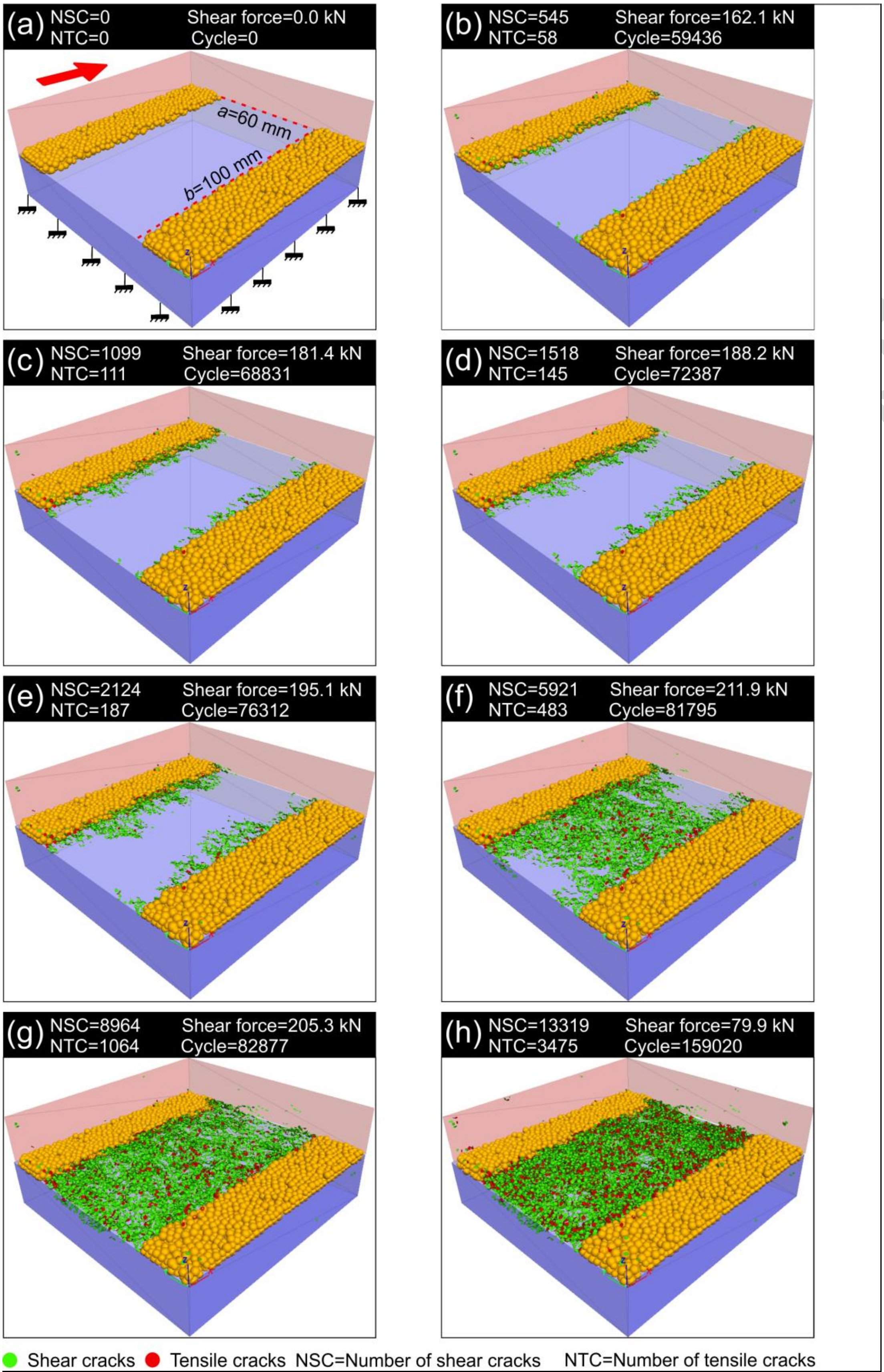
(a) NSC=0 NTC=0 Shear force=0.0 kN Cycle=0
a=60 mm
b=100 mm
(b) NSC=545 NTC=58 Shear force=162.1 kN Cycle=59436
(c) NSC=1099 NTC=111 Shear force=181.4 kN Cycle=68831
(d) NSC=1518 NTC=145 Shear force=188.2 kN Cycle=72387
(e) NSC=2124 NTC=187 Shear force=195.1 kN Cycle=76312
(f) NSC=5921 NTC=483 Shear force=211.9 kN Cycle=81795
(g) NSC=8964 NTC=1064 Shear force=205.3 kN Cycle=82877
(h) NSC=13319 NTC=3475 Shear force=79.9 kN Cycle=159020
Shear cracks
Tensile cracks
NSC=Number of shear cracks
NTC=Number of tensile cracks

Fig 6

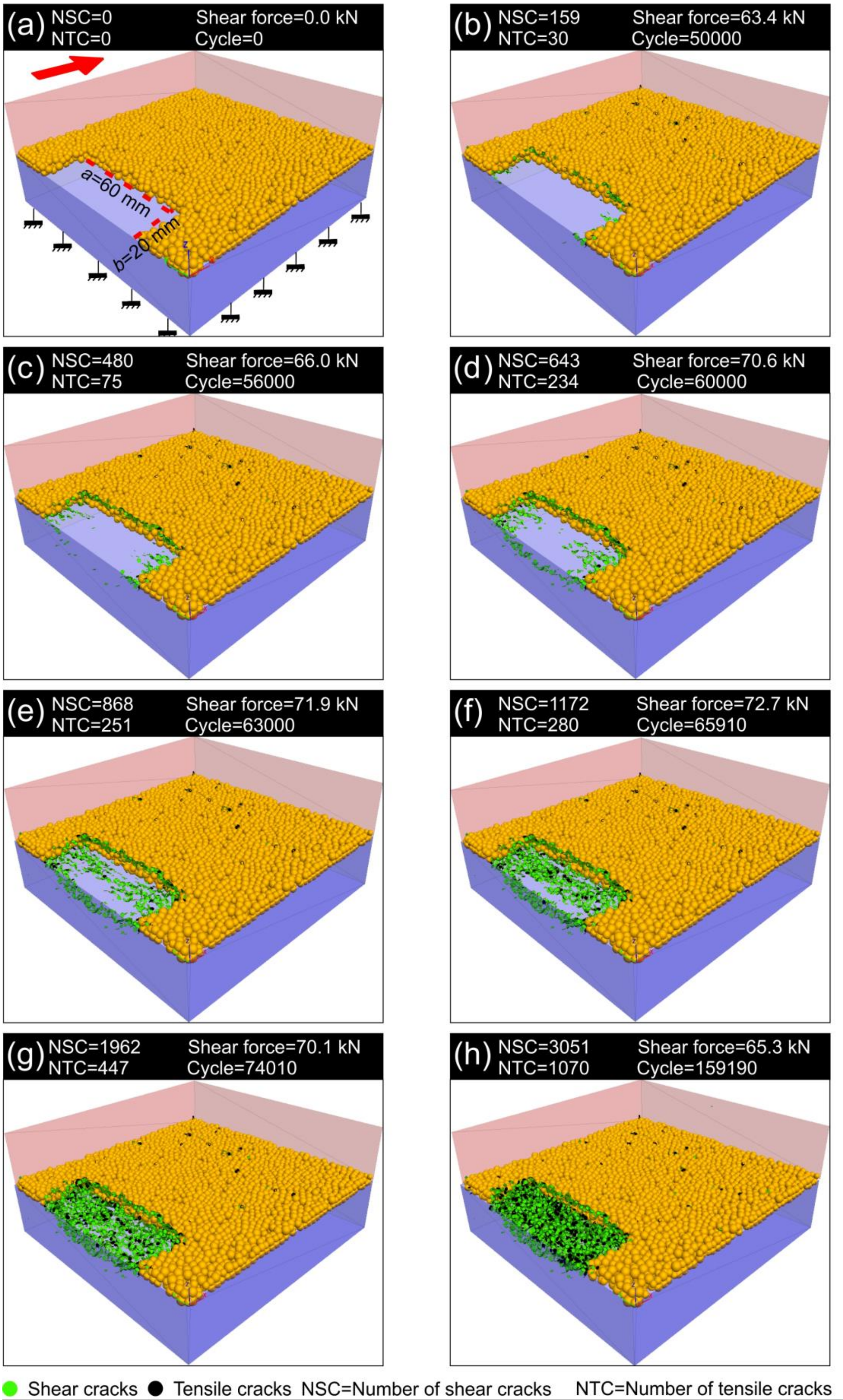
(a) NSC=0
NTC=0
Shear force=0.0 kN
Cycle=0
a=60 mm
b=20 mm
(b) NSC=159
NTC=30
Shear force=63.4 kN
Cycle=50000
(c) NSC=480
NTC=75
Shear force=66.0 kN
Cycle=56000
(d) NSC=643
NTC=234
Shear force=70.6 kN
Cycle=60000
(e) NSC=868
NTC=251
Shear force=71.9 kN
Cycle=63000
(f) NSC=1172
NTC=280
Shear force=72.7 kN
Cycle=65910
(g) NSC=1962
NTC=447
Shear force=70.1 kN
Cycle=74010
(h) NSC=3051
NTC=1070
Shear force=65.3 kN
Cycle=159190
Shear cracks
Tensile cracks
NSC=Number of shear cracks
NTC=Number of tensile cracks

Fig 7

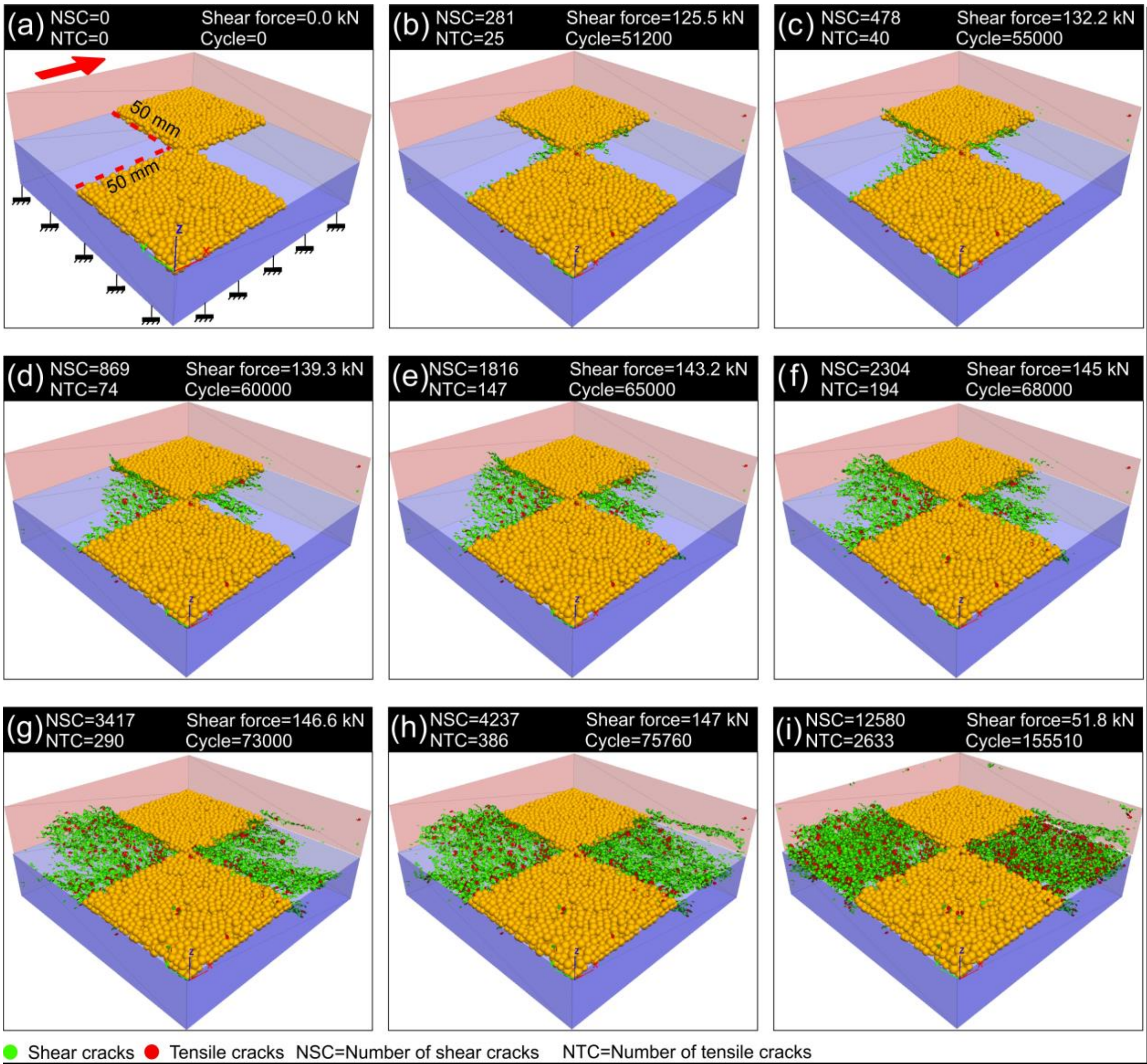

(a) NSC=0 NTC=0 Shear force=0.0 kN Cycle=0
50 mm
50 mm
(b) NSC=281 NTC=25 Shear force=125.5 kN Cycle=51200
(c) NSC=478 NTC=40 Shear force=132.2 kN Cycle=55000
(d) NSC=869 NTC=74 Shear force=139.3 kN Cycle=60000
(e) NSC=1816 NTC=147 Shear force=143.2 kN Cycle=65000
(f) NSC=2304 NTC=194 Shear force=145 kN Cycle=68000
(g) NSC=3417 NTC=290 Shear force=146.6 kN Cycle=73000
(h) NSC=4237 NTC=386 Shear force=147 kN Cycle=75760
(i) NSC=12580 NTC=2633 Shear force=51.8 kN Cycle=155510
Shear cracks Tensile cracks NSC=Number of shear cracks NTC=Number of tensile cracks

Fig 8

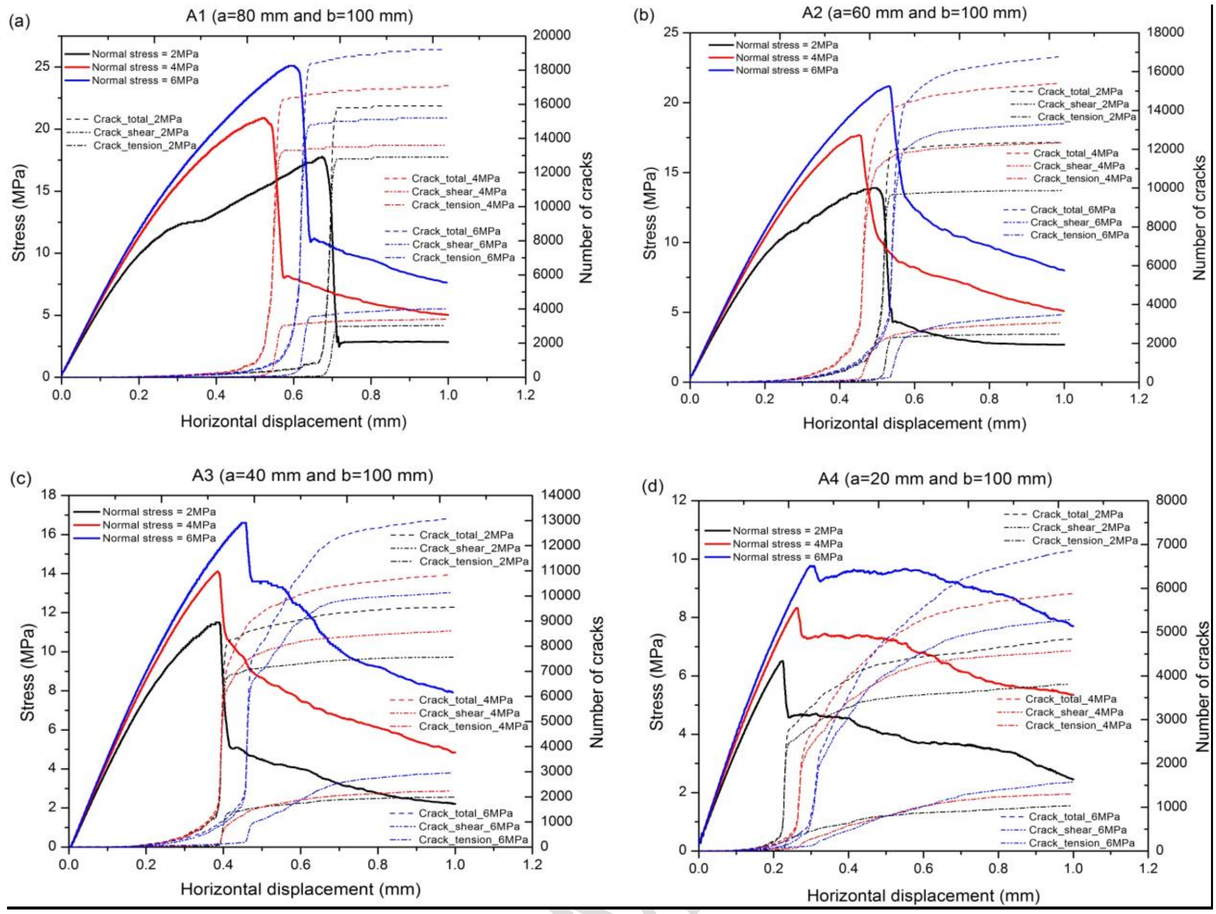
(a)
A1 (a=80 mm and b=100 mm)
Normal stress = 2MPa
Normal stress = 4MPa
Normal stress = 6MPa
Crack_total_2MPa
Crack_shear_2MPa
Crack_tension_2MPa
Crack_total_4MPa
Crack_shear_4MPa
Crack_tension_4MPa
Crack_total_6MPa
Crack_shear_6MPa
Crack_tension_6MPa
Stress (MPa)
Number of cracks
Horizontal displacement (mm)
(b)
A2 (a=60 mm and b=100 mm)
Normal stress = 2MPa
Normal stress = 4MPa
Normal stress = 6MPa
Crack_total_2MPa
Crack_shear_2MPa
Crack_tension_2MPa
Crack_total_4MPa
Crack_shear_4MPa
Crack_tension_4MPa
Crack_total_6MPa
Crack_shear_6MPa
Crack_tension_6MPa
Stress (MPa)
Number of cracks
Horizontal displacement (mm)
(c)
A3 (a=40 mm and b=100 mm)
Normal stress = 2MPa
Normal stress = 4MPa
Normal stress = 6MPa
Crack_total_2MPa
Crack_shear_2MPa
Crack_tension_2MPa
Crack_total_4MPa
Crack_shear_4MPa
Crack_tension_4MPa
Crack_total_6MPa
Crack_shear_6MPa
Crack_tension_6MPa
Stress (MPa)
Number of cracks
Horizontal displacement (mm)
(d)
A4 (a=20 mm and b=100 mm)
Normal stress = 2MPa
Normal stress = 4MPa
Normal stress = 6MPa
Crack_total_2MPa
Crack_shear_2MPa
Crack_tension_2MPa
Crack_total_4MPa
Crack_shear_4MPa
Crack_tension_4MPa
Crack_total_6MPa
Crack_shear_6MPa
Crack_tension_6MPa
Stress (MPa)
Number of cracks
Horizontal displacement (mm)

Fig 9

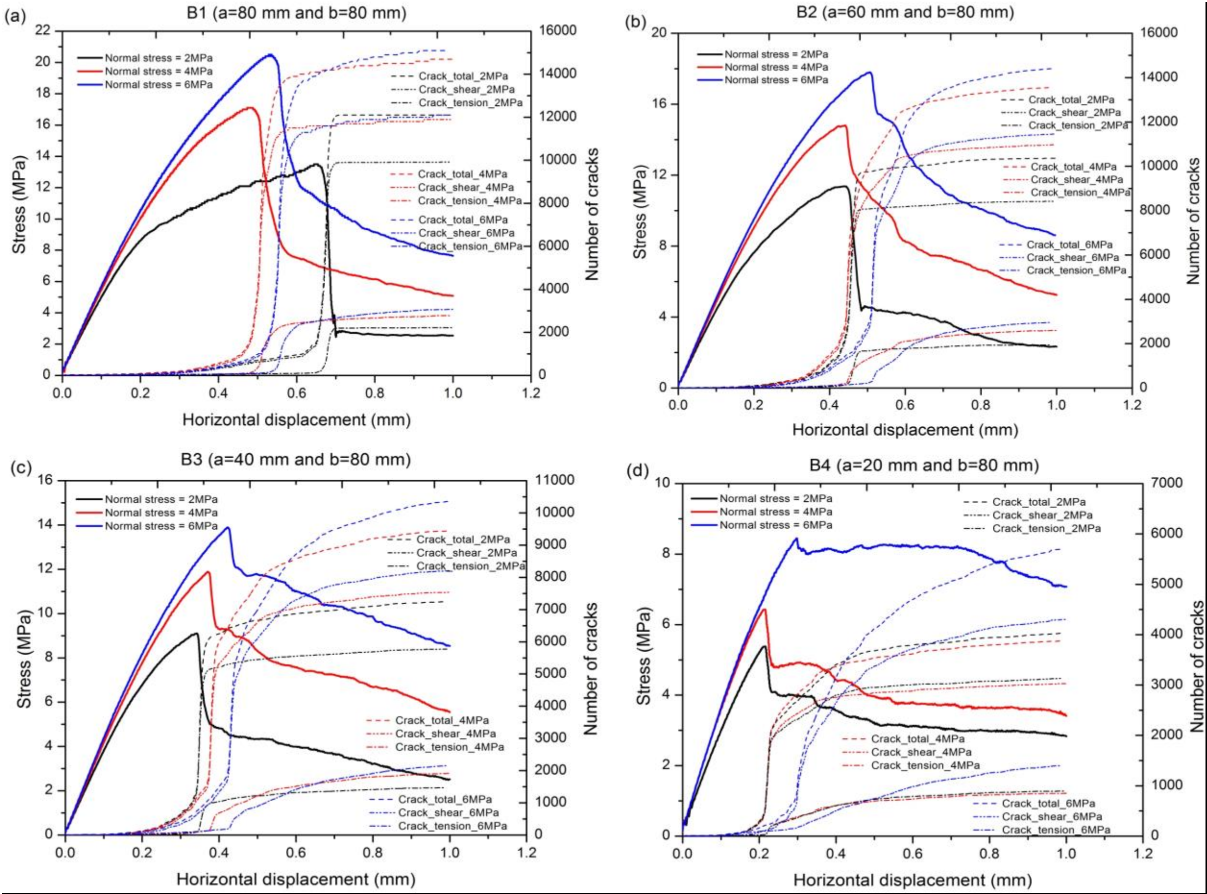
(a)
B1 (a=80 mm and b=80 mm)
Normal stress = 2MPa
Normal stress = 4MPa
Normal stress = 6MPa
Crack_total_2MPa
Crack_shear_2MPa
Crack_tension_2MPa
Crack_total_4MPa
Crack_shear_4MPa
Crack_tension_4MPa
Crack_total_6MPa
Crack_shear_6MPa
Crack_tension_6MPa
Stress (MPa)
Number of cracks
Horizontal displacement (mm)
(b)
B2 (a=60 mm and b=80 mm)
Normal stress = 2MPa
Normal stress = 4MPa
Normal stress = 6MPa
Crack_total_2MPa
Crack_shear_2MPa
Crack_tension_2MPa
Crack_total_4MPa
Crack_shear_4MPa
Crack_tension_4MPa
Crack_total_6MPa
Crack_shear_6MPa
Crack_tension_6MPa
Stress (MPa)
Number of cracks
Horizontal displacement (mm)
(c)
B3 (a=40 mm and b=80 mm)
Normal stress = 2MPa
Normal stress = 4MPa
Normal stress = 6MPa
Crack_total_2MPa
Crack_shear_2MPa
Crack_tension_2MPa
Crack_total_4MPa
Crack_shear_4MPa
Crack_tension_4MPa
Crack_total_6MPa
Crack_shear_6MPa
Crack_tension_6MPa
Stress (MPa)
Number of cracks
Horizontal displacement (mm)
(d)
B4 (a=20 mm and b=80 mm)
Normal stress = 2MPa
Normal stress = 4MPa
Normal stress = 6MPa
Crack_total_2MPa
Crack_shear_2MPa
Crack_tension_2MPa
Crack_total_4MPa
Crack_shear_4MPa
Crack_tension_4MPa
Crack_total_6MPa
Crack_shear_6MPa
Crack_tension_6MPa
Stress (MPa)
Number of cracks
Horizontal displacement (mm)

Fig 10

.

924

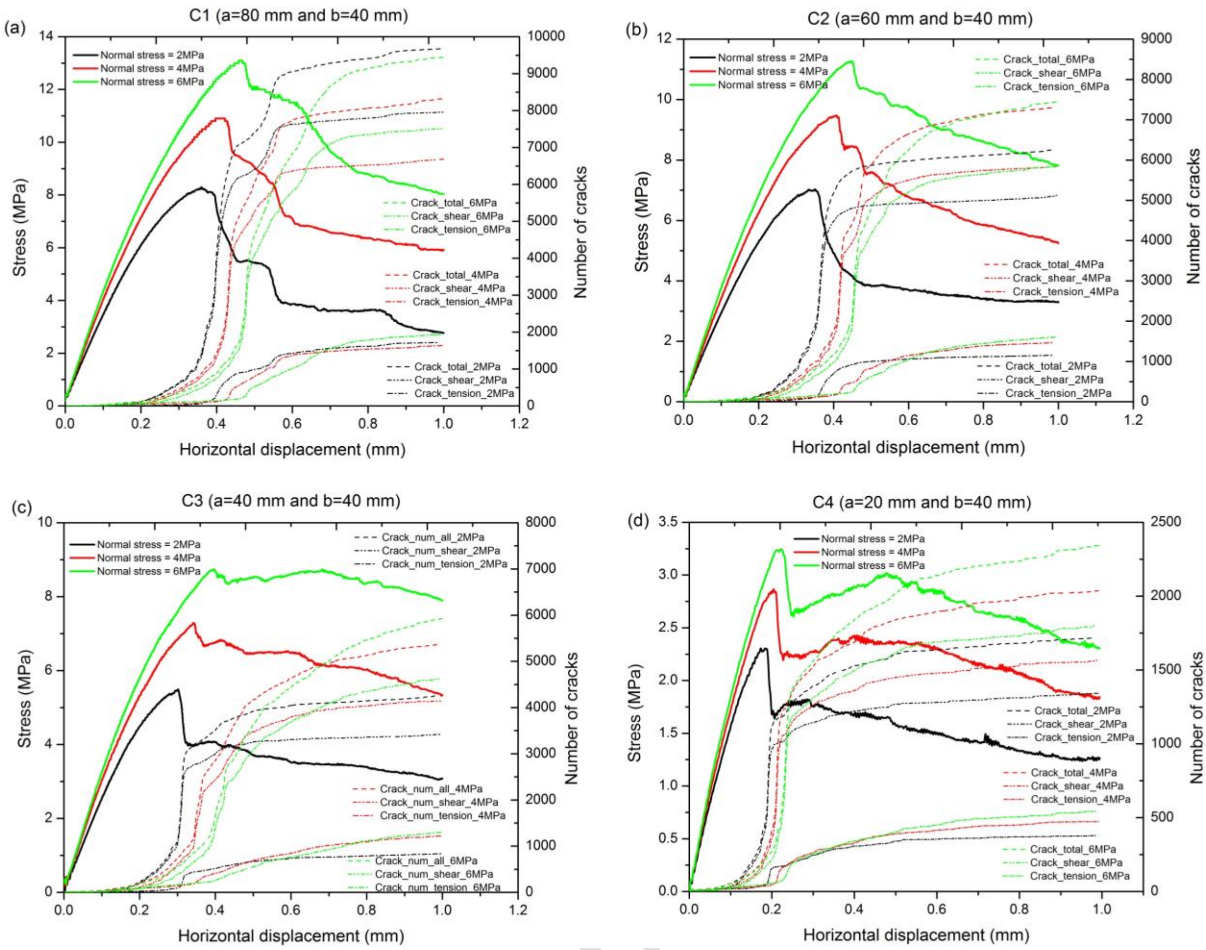

925 **Fig 11**

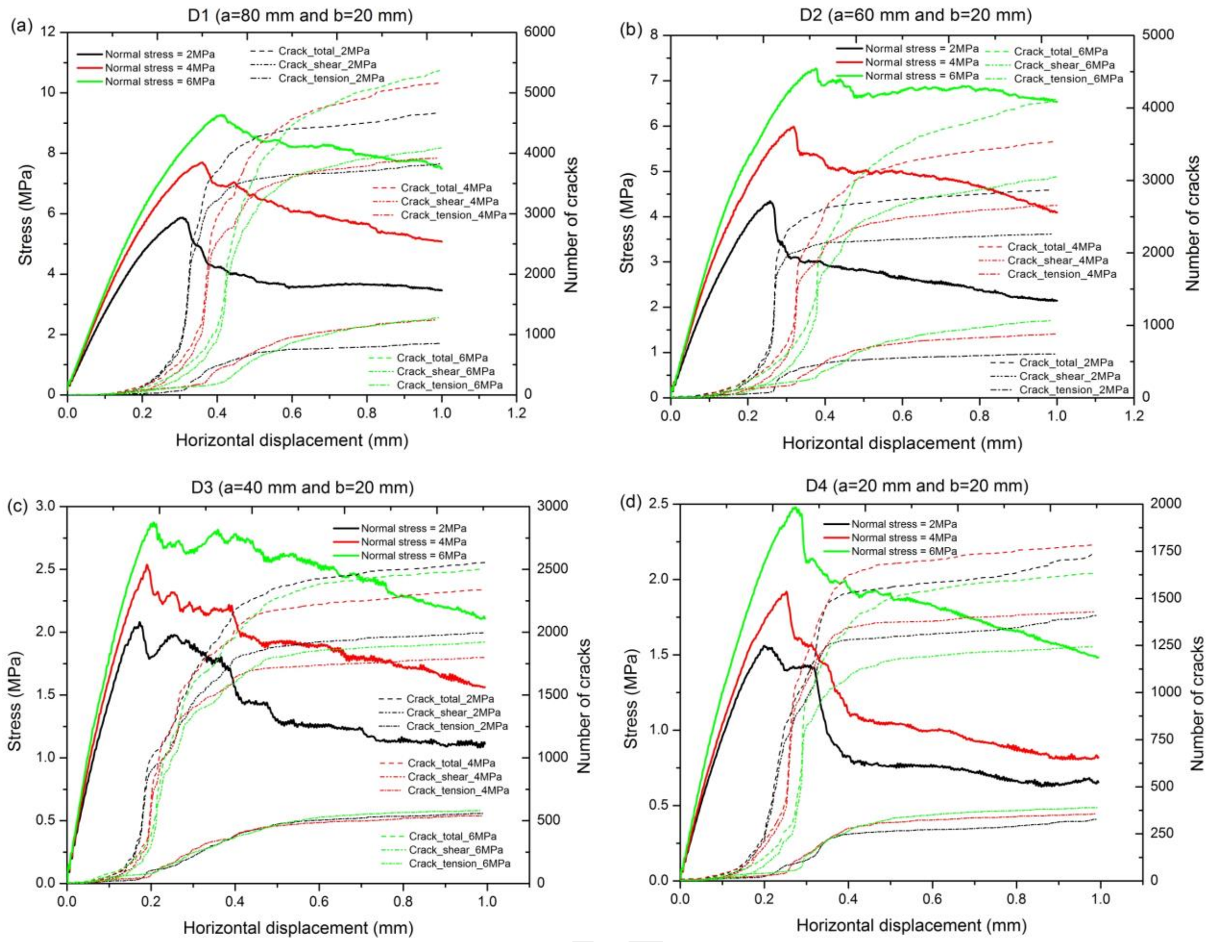
(a)
D1 (a=80 mm and b=20 mm)
Normal stress = 2MPa
Normal stress = 4MPa
Normal stress = 6MPa
Crack_total_2MPa
Crack_shear_2MPa
Crack_tension_2MPa
Crack_total_4MPa
Crack_shear_4MPa
Crack_tension_4MPa
Crack_total_6MPa
Crack_shear_6MPa
Crack_tension_6MPa
Stress (MPa)
Number of cracks
Horizontal displacement (mm)
(b)
D2 (a=60 mm and b=20 mm)
Normal stress = 2MPa
Normal stress = 4MPa
Normal stress = 6MPa
Crack_total_6MPa
Crack_shear_6MPa
Crack_tension_6MPa
Crack_total_4MPa
Crack_shear_4MPa
Crack_tension_4MPa
Crack_total_2MPa
Crack_shear_2MPa
Crack_tension_2MPa
Stress (MPa)
Number of cracks
Horizontal displacement (mm)
(c)
D3 (a=40 mm and b=20 mm)
Normal stress = 2MPa
Normal stress = 4MPa
Normal stress = 6MPa
Crack_total_2MPa
Crack_shear_2MPa
Crack_tension_2MPa
Crack_total_4MPa
Crack_shear_4MPa
Crack_tension_4MPa
Crack_total_6MPa
Crack_shear_6MPa
Crack_tension_6MPa
Stress (MPa)
Number of cracks
Horizontal displacement (mm)
(d)
D4 (a=20 mm and b=20 mm)
Normal stress = 2MPa
Normal stress = 4MPa
Normal stress = 6MPa
Stress (MPa)
Number of cracks
Horizontal displacement (mm)

Fig 12

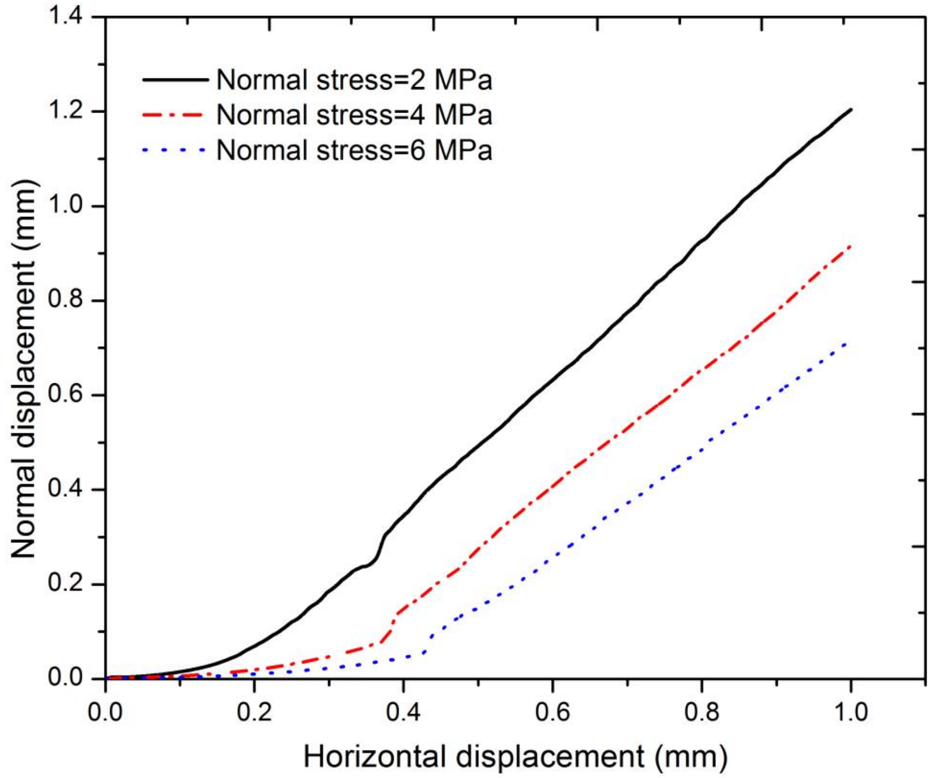

928

929 **Fig 13**

930

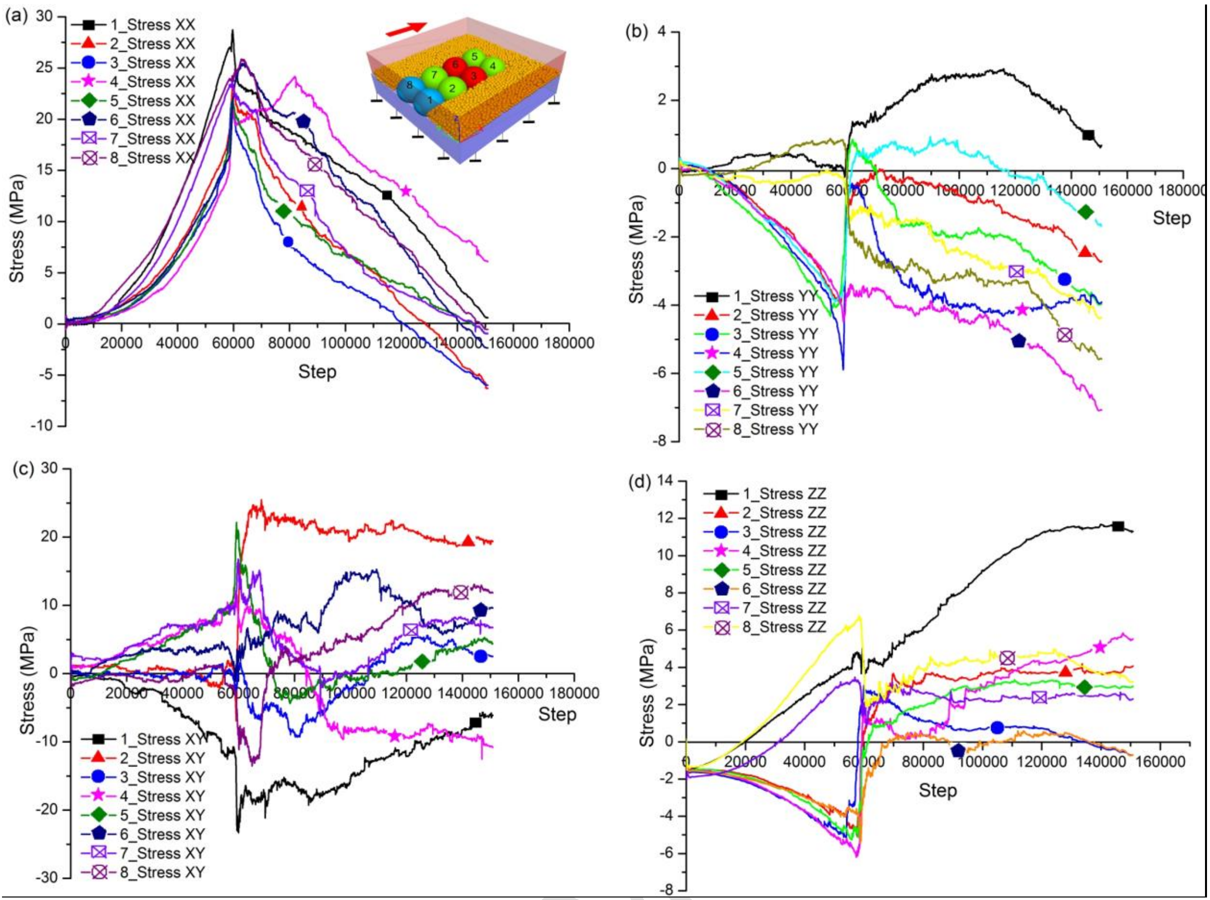
(a)
1_Stress XX
2_Stress XX
3_Stress XX
4_Stress XX
5_Stress XX
6_Stress XX
7_Stress XX
8_Stress XX
Stress (MPa)
Step
(b)
1_Stress YY
2_Stress YY
3_Stress YY
4_Stress YY
5_Stress YY
6_Stress YY
7_Stress YY
8_Stress YY
Stress (MPa)
Step
(c)
1_Stress XY
2_Stress XY
3_Stress XY
4_Stress XY
5_Stress XY
6_Stress XY
7_Stress XY
8_Stress XY
Stress (MPa)
Step
(d)
1_Stress ZZ
2_Stress ZZ
3_Stress ZZ
4_Stress ZZ
5_Stress ZZ
6_Stress ZZ
7_Stress ZZ
8_Stress ZZ
Stress (MPa)
Step

Fig 14

933

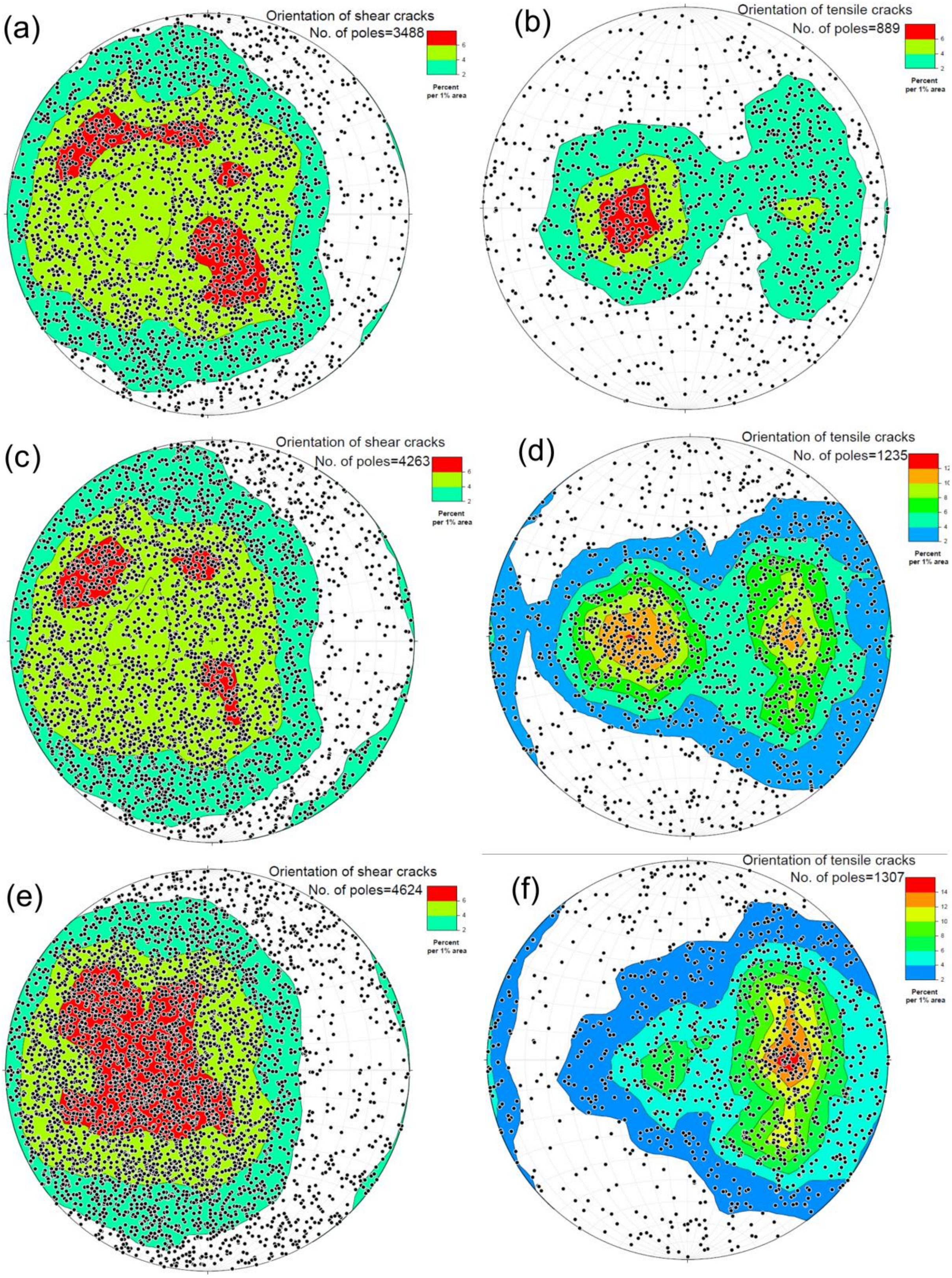

934 **Fig 15**

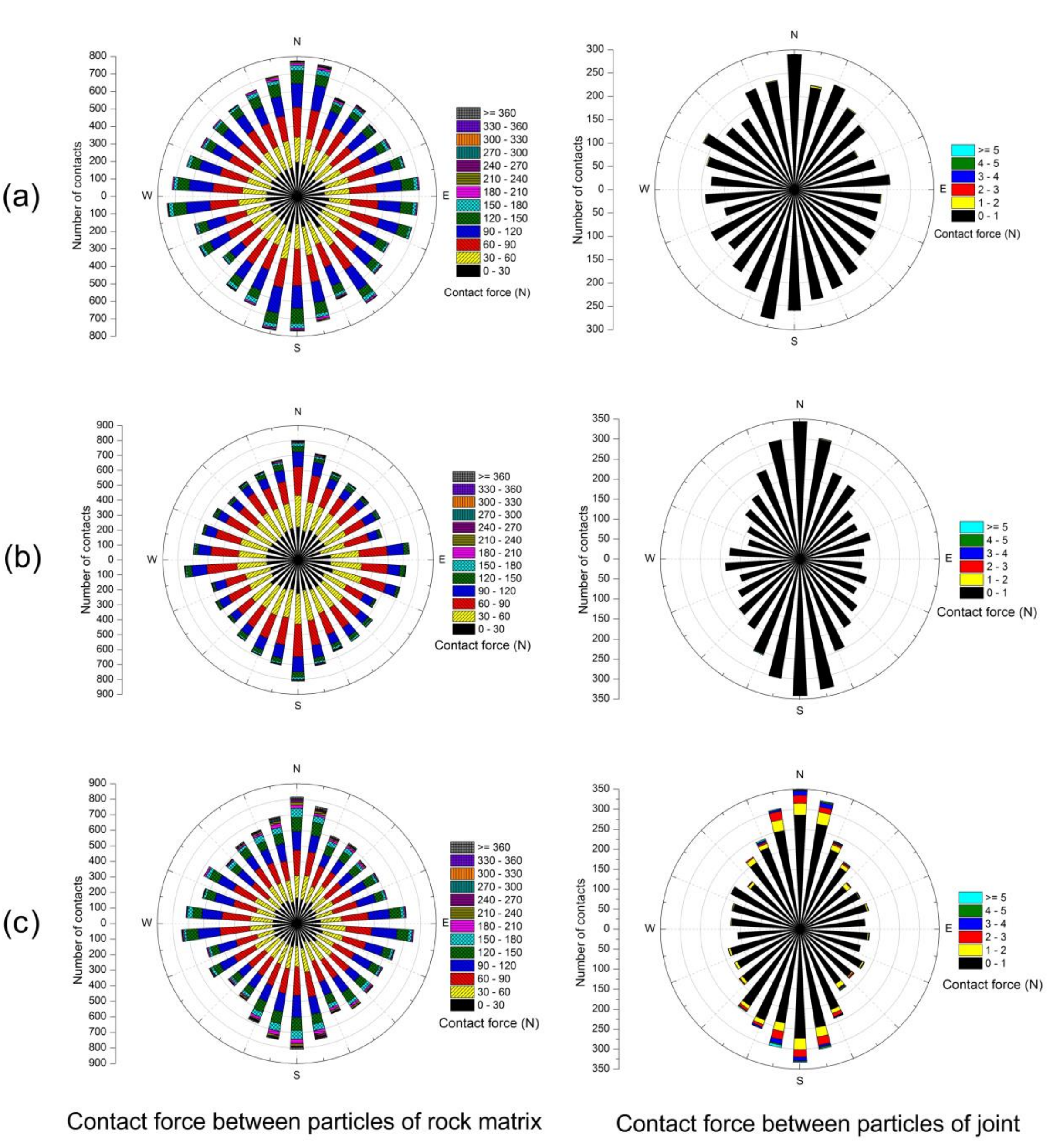
(a)
(b)
(c)
N
S
E
W
Number of contacts
>= 360
330 - 360
300 - 330
270 - 300
240 - 270
210 - 240
180 - 210
150 - 180
120 - 150
90 - 120
60 - 90
30 - 60
0 - 30
Contact force (N)
>= 5
4 - 5
3 - 4
2 - 3
1 - 2
0 - 1
Contact force between particles of rock matrix
Contact force between particles of joint

Fig 16

937

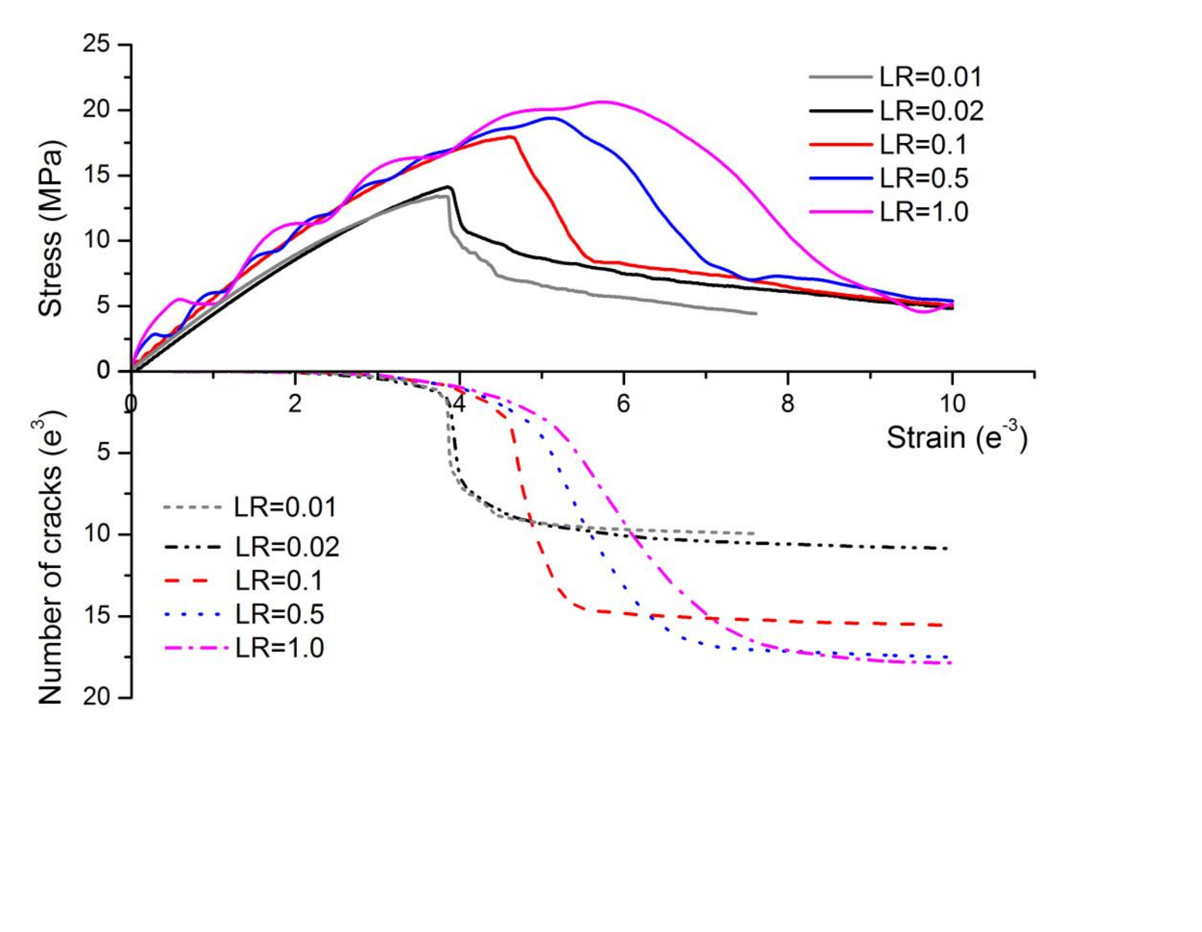

938 **Fig 17a**

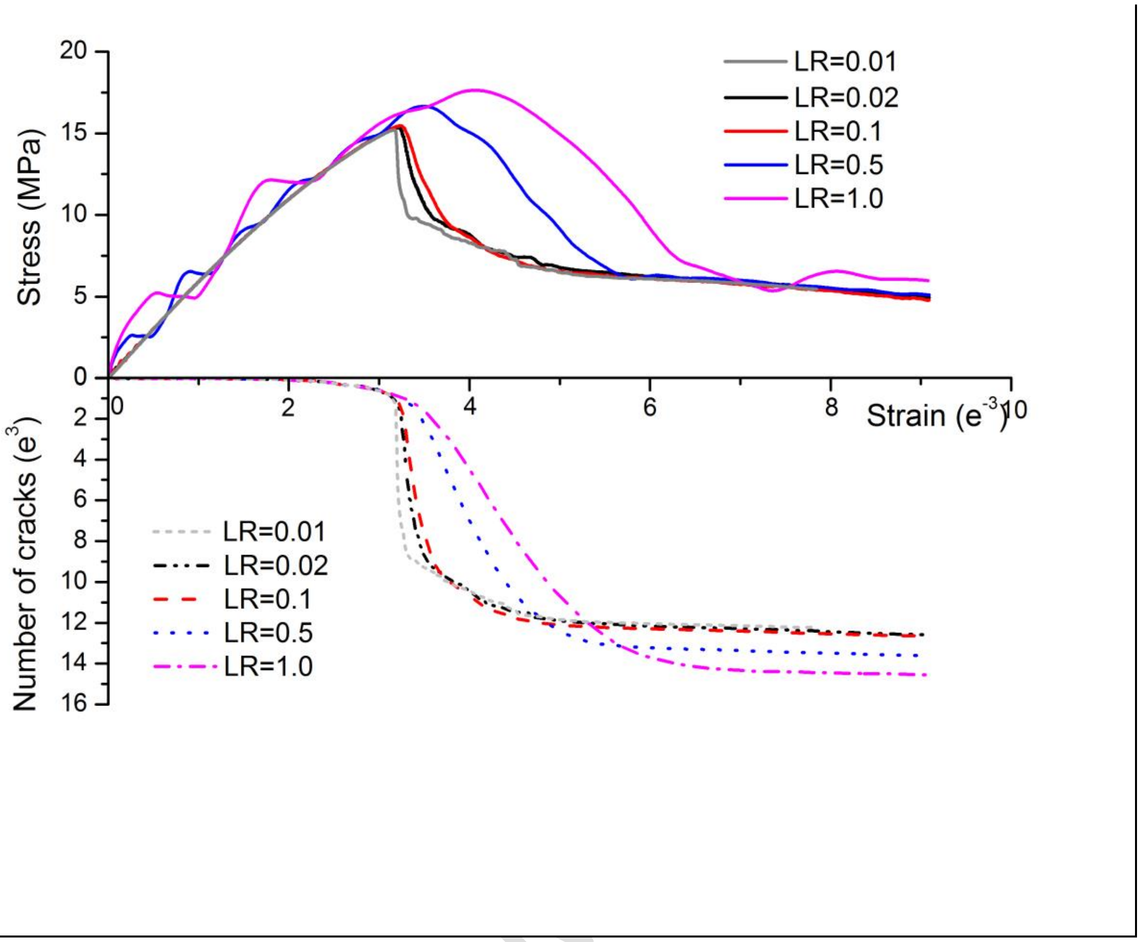

Stress (MPa)
20
15
10
5
0
LR=0.01
LR=0.02
LR=0.1
LR=0.5
LR=1.0
0
2
4
6
8
Strain (e-3) 10
Number of cracks (e3)
2
4
6
8
10
12
14
16
LR=0.01
LR=0.02
LR=0.1
LR=0.5
LR=1.0

940 **Fig 17b**

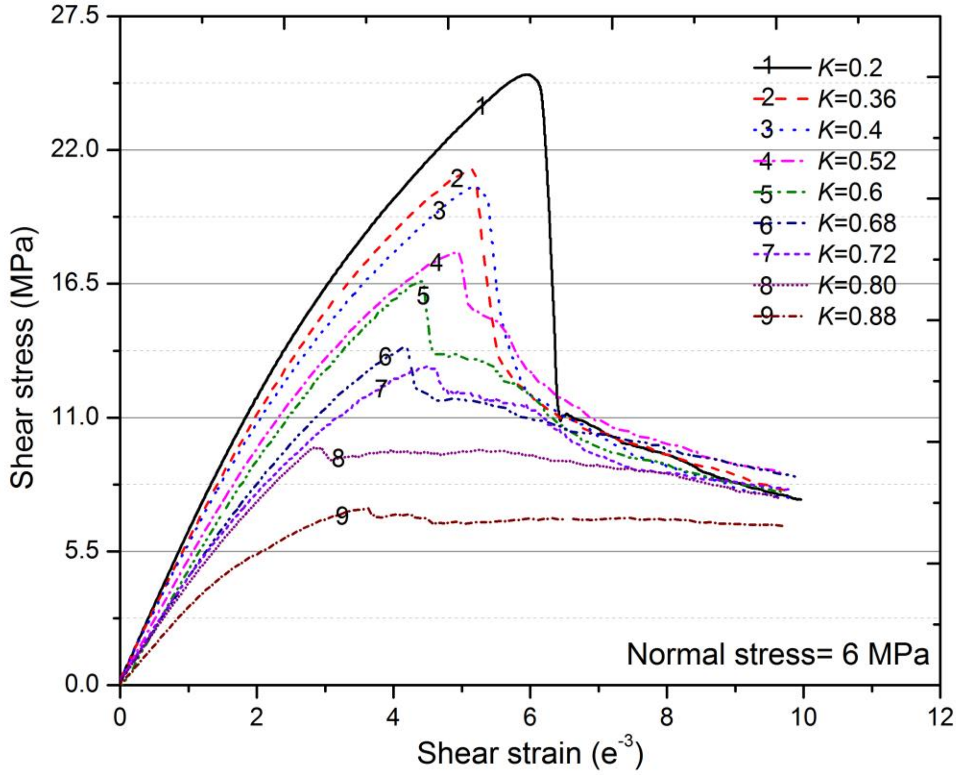
27.5
22.0
16.5
11.0
5.5
0.0
Shear stress (MPa)
0
2
4
6
8
10
12
Shear strain (e-3)
1 K=0.2
2 K=0.36
3 K=0.4
4 K=0.52
5 K=0.6
6 K=0.68
7 K=0.72
8 K=0.80
9 K=0.88
Normal stress= 6 MPa

Fig 18

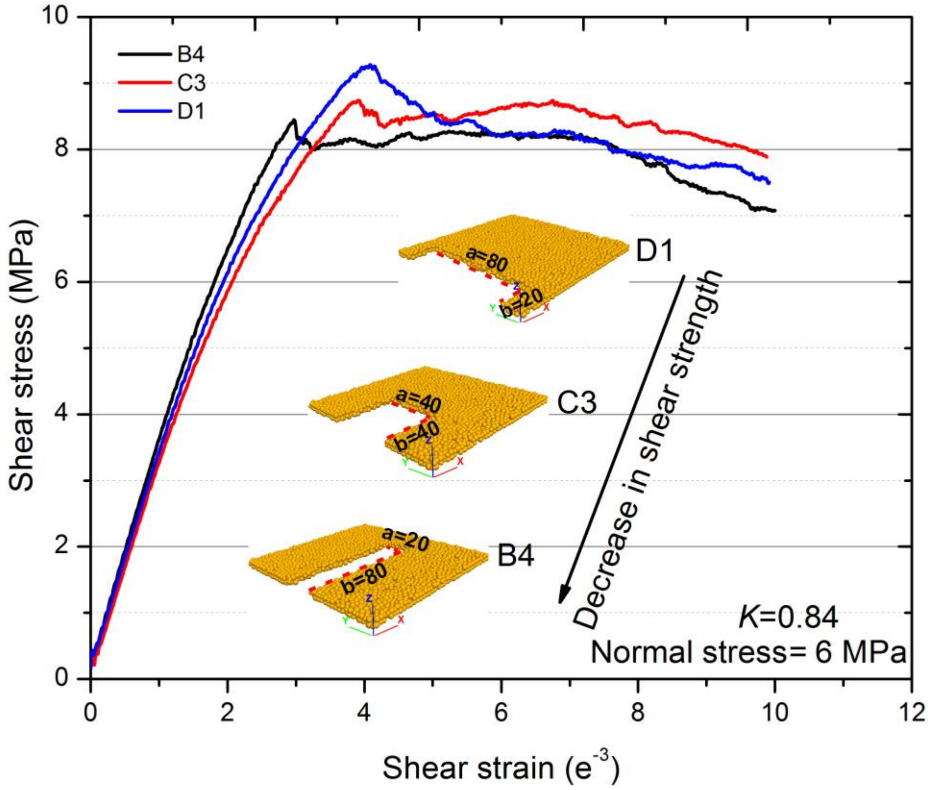

B4
C3
D1
Shear stress (MPa)
Shear strain (e^-3)
a=80
b=20
D1
a=40
b=40
C3
a=20
b=80
B4
Decrease in shear strength
K=0.84
Normal stress= 6 MPa

Fig 19

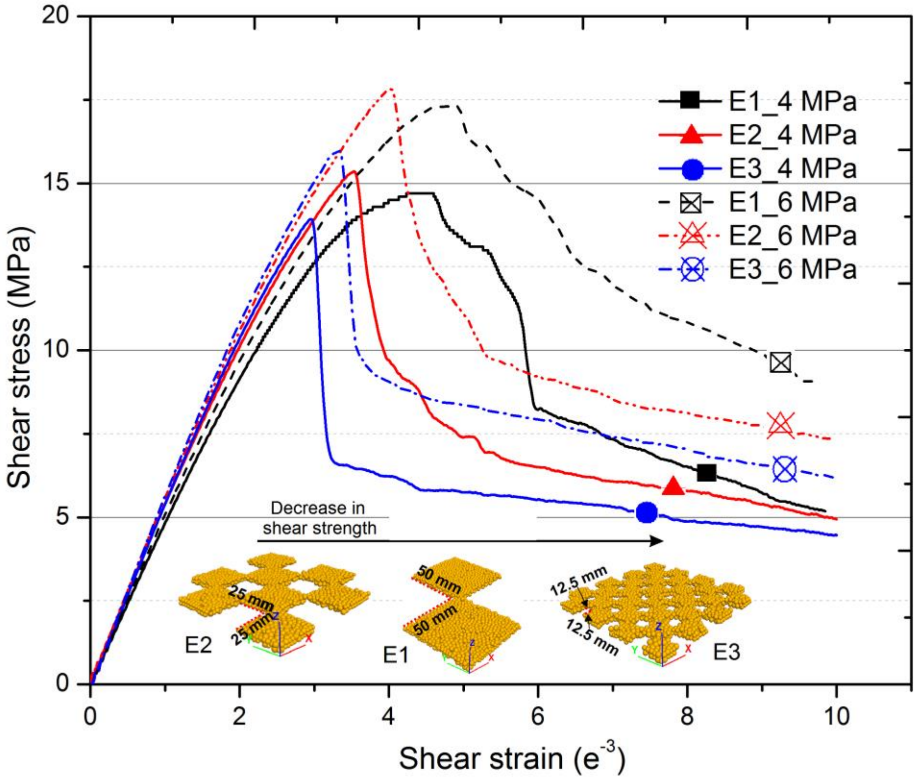
Shear stress (MPa)
Shear strain (e^{-3})
E1_4 MPa
E2_4 MPa
E3_4 MPa
E1_6 MPa
E2_6 MPa
E3_6 MPa
Decrease in
shear strength
E2
E1
E3
25 mm
25 mm
50 mm
50 mm
12.5 mm
12.5 mm
0
5
10
15
20
0
2
4
6
8
10

Fig 20